

## GAMMA-RAY BURST EARLY AFTERGLOWS: REVERSE SHOCK EMISSION FROM AN ARBITRARILY MAGNETIZED EJECTA

BING ZHANG<sup>1</sup> AND SHIHO KOBAYASHI<sup>2,3</sup>

Received 2004 April 7; accepted 2005 February 18

### ABSTRACT

Evidence suggests that gamma-ray burst (GRB) ejecta are likely magnetized, although the degree of magnetization is unknown. When such magnetized ejecta are decelerated by the ambient medium, the characteristics of the reverse shock emission are strongly influenced by the degree of magnetization. We derive a rigorous analytical solution for the relativistic  $90^\circ$  shocks under the ideal MHD condition. The solution is reduced to the Blandford-McKee hydrodynamical solution when the magnetization parameter  $\sigma$  approaches zero, and to the Kennel-Coroniti solution (which depends on  $\sigma$  only) when the shocks upstream and downstream are ultrarelativistic with respect to each other. Our generalized solution can be used to treat the more general cases, e.g., when the shocks upstream and downstream are mildly relativistic with respect to each other. We find that the suppression factor of the shock in the strong magnetic field regime is only mild as long as the shock upstream is relativistic with respect to the downstream, and it saturates in the high- $\sigma$  regime. This indicates that generally strong relativistic shocks still exist in the high- $\sigma$  limit. This can effectively convert kinetic energy into heat. The overall efficiency of converting ejecta energy into heat, however, decreases with increasing  $\sigma$ , mainly because the fraction of the kinetic energy in the total energy decreases. We use the theory to study the reverse shock emission properties of arbitrarily magnetized ejecta in the GRB problem assuming a constant density of the circumburst medium. We study the shell-medium interaction in detail and categorize various critical radii for shell evolution. With typical GRB parameters, a reverse shock exists when  $\sigma$  is less than a few tens or a few hundreds. The shell evolution can still be categorized into the thick and thin shell regimes, but the separation between the two regimes now depends on the  $\sigma$ -parameter and the thick shell regime greatly shrinks at high  $\sigma$ . The thin shell regime can also be categorized into two subregions depending on whether the shell starts to spread during the first shock crossing. The early optical afterglow light curves are calculated for GRBs with a wide range of  $\sigma$ -value, with the main focus on the reverse shock component. We find that as  $\sigma$  increases from below, the reverse shock emission level increases steadily until reaching a peak at  $\sigma \lesssim 1$ , then it decreases steadily when  $\sigma > 1$ . At large  $\sigma$ -values, the reverse shock peak is broadened in the thin shell regime because of the separation of the shock crossing radius and the deceleration radius. This novel feature can be regarded as a signature of high  $\sigma$ . The early afterglow data of GRB 990123 and GRB 021211 could be understood within the theoretical framework developed in this paper, with the inferred  $\sigma$ -value  $\gtrsim 0.1$ . The case of GRB 021004 and GRB 030418 may be also interpreted with higher  $\sigma$ -values, although more detailed modeling is needed. Early tight optical upper limits could be interpreted as very high  $\sigma$  cases, in which a reverse shock does not exist or is very weak. Our model predictions could be further tested against future abundant early afterglow data collected by the *Swift* UV-optical telescope, so that the magnetic content of GRB fireballs can be diagnosed.

*Subject headings:* gamma rays: bursts — radiation mechanisms: nonthermal — shock waves — stars: magnetic fields

### 1. INTRODUCTION

Extensive broadband observational campaigns and theoretical modeling of gamma-ray burst (GRB) afterglows have greatly advanced our understanding of these mysterious cosmic explosions. Yet, the origin of the GRB prompt emission itself and the nature of the relativistic flow (which are directly connected to the function of the central engine) are still unknown (e.g., Mészáros 2002; Zhang & Mészáros 2004). In particular, it is unclear how important the role of magnetic fields is in producing GRBs. Recently, two independent pieces of evidence suggested that the GRB central engine is likely strongly magnetized. First, the claimed detection of a very high degree of linear polarization of gamma-ray emission in GRB 021206 (Coburn & Boggs 2003;

see however Rutledge & Fox 2004), if true, could be readily interpreted by assuming that the magnetic field involved in the synchrotron radiation is globally ordered (e.g., Waxman 2003; Granot 2003), although some alternative explanations remain (e.g., Waxman 2003). Second, recently we (Zhang et al. 2003, hereafter ZKM03) developed a method to perform a combined reverse and forward shock emission study for GRB early optical afterglows and revealed that a stronger magnetic field in the reverse shock region than in the forward shock region is needed to interpret the early afterglow data of GRB 990123 and GRB 021211. This claim was confirmed by independent detailed case studies for both bursts (Fan et al. 2002; Kumar & Panaitescu 2003). These findings suggest that magnetic fields may play a significant role in the GRB physics, as has been suggested by various authors previously (e.g., Usov 1994; Thompson 1994; Mészáros & Rees 1997b; Wheeler et al. 2000; Spruit et al. 2001; Blandford 2002). Within the framework of the currently favored collapsar progenitor model for GRBs (MacFadyen & Woosley 1999), the ejecta are found to be magnetized when MHD simulations are performed (Proga et al. 2003).

<sup>1</sup> Department of Physics, University of Nevada, Las Vegas, NV 89154.

<sup>2</sup> Department of Astronomy and Astrophysics, Pennsylvania State University, University Park, PA 16802.

<sup>3</sup> Department of Physics, Pennsylvania State University, University Park, PA 16802.

The degree of magnetization of the ejecta, however, is unknown. This is usually quantified by the parameter  $\sigma$  (see eq. [7] for a precise definition), the ratio of the electromagnetic energy flux to the kinetic energy flux. Current GRB models are focused on two extreme regimes. In the first regime, it is essentially assumed that the GRB fireball is purely hydrodynamical. Magnetic fields are introduced only through an equipartition parameter  $\epsilon_B$  (which is of the order of 0.001–0.1) for the purpose of calculating synchrotron radiation. This is the  $\sigma \rightarrow 0$  regime. In this picture, the GRB prompt emission is produced from internal shocks (Rees & Mészáros 1994) or sometimes from external shocks (Mészáros & Rees 1993; Dermer & Mitman 1999). This is currently the standard scenario of GRB emission. The second is the  $\sigma \rightarrow \infty$  regime. This is the regime in which a Poynting flux dominates the flow, and GRB prompt emission is envisaged to be due to some less familiar magnetic dissipation processes (e.g., Usov 1994; Spruit et al. 2001; Blandford 2002; Lyutikov & Blandford 2003). In principle, a GRB event could include both a “hot component” as invoked in the  $\sigma = 0$  model (e.g., due to neutrino annihilation) and a “cold component” as invoked in the  $\sigma = \infty$  model; the interplay between both components may result in a  $\sigma$ -value that varies over a wide range (Zhang & Mészáros 2002). It is an important but difficult task to pin down the degree of magnetization of GRB ejecta.

GRB early afterglow data (especially in the optical band) potentially contain essential information for diagnosing the magnetic content of the fireball. The reason is that an early optical afterglow light curve is believed to include contributions from both the forward shock (which propagates into the ambient medium) and the reverse shock (which propagates into the ejecta itself). Since the degree of magnetization of the ejecta influences the emission level of the reverse shock (or maybe even the level of the forward shock), by studying the interplay between the reverse shock and the forward shock emission components, one could potentially infer the degree of magnetization of the ejecta. In all the current analyses, the reverse shock emission is treated purely hydrodynamically (e.g., Mészáros & Rees 1997a; Sari & Piran 1999; Kobayashi 2000; Kobayashi & Zhang 2003a; ZKM03). When confronted with the available early afterglow data (four cases so far: GRB 990123, Akerlof et al. 1999; GRB 021004, Fox et al. 2003a; GRB 021211, Fox et al. 2003b, Li et al. 2003a; and GRB 030418, Rykoff et al. 2004), the model works reasonably well for two of them (GRB 990123 and GRB 021211), although a good fit requires that the magnetic field in the reverse shock region be much stronger than that in the forward shock region (ZKM03). For the other two, the light curves are not easy to explain with the simplest reverse shock model. On the other hand, GRB ejecta could in principle have an arbitrary  $\sigma$ -value. When  $\sigma$  is large, the conventional hydrodynamical treatment is no longer a good approximation, and a full treatment involving MHD shock jump conditions is desirable.

It is generally believed that a GRB involves a rapidly rotating central engine. If the magnetic dissipation processes are not significant, field lines are essentially frozen in the expanding shells. The radial component of the magnetic field decays with radius as  $\propto R^{-2}$ , while the toroidal magnetic field decays as  $\sim R^{-1}$ . At the external shock radius, magnetic field lines are essentially frozen in the plane perpendicular to the moving direction. The MHD shock Rankine-Hugoniot relations are greatly simplified in such a  $90^\circ$  shock. Such relations have been studied extensively before, both analytically and numerically. Kennel & Coroniti (1984) derived some simplified analytical expressions applicable for strong  $90^\circ$  shocks whose upstream and downstream are ultra-relativistic with respect to each other. The model was used to

treat the pulsar wind nebula problem. In this regime, the strength of the shock is essentially characterized by only one parameter, i.e., the  $\sigma$ -parameter. The conclusion was later confirmed by numerical simulations (e.g., Gallant et al. 1992).

Within the context of GRBs, since a GRB invokes a transient release of energy, the ejecta shell has a finite width (in contrast to the long-standing pulsar wind). Under some conditions, the reverse shocks upstream and downstream could never become relativistic with respect to each other when the reverse shock crosses the ejecta shell. In the  $\sigma = 0$  limit, whether the reverse shock becomes relativistic depends on the comparison between the timescale ( $T$ ) of the central engine activity (essentially the duration of the burst) and the timescale ( $t_\gamma$ ) when the mass of the ambient medium collected by the fireball reaches  $1/\gamma_0$  times the mass of the ejecta (e.g., Sari & Piran 1995; Kobayashi et al. 1999). Both times are measured by the observer. The case of  $T > t_\gamma$  is called the thick shell regime, and the reverse shock is relativistic. In many cases, however, one has  $T < t_\gamma$ , i.e., the thin shell regime.<sup>4</sup> The reverse shock is initially nonrelativistic and only becomes mildly relativistic as the shock crosses the shell. For magnetized ejecta (e.g., a shell with a finite width but an arbitrary  $\sigma$ -value), the separation between the thick and thin shell regimes becomes more complicated, but the nonrelativistic reverse shock case (for the thin shell regime) is even more common (see § 3.3). The Kennel-Coroniti approximation cannot be used directly. The theory developed in this paper becomes essential for discussing the reverse shock physics in this parameter regime.

In this paper, we present a detailed treatment of reverse shock emission for an arbitrarily magnetized ejecta under the ideal MHD condition. The reverse shock emission in the mildly magnetized regime was also recently discussed by Fan et al. (2004a). Here we develop a theoretical framework to include discussions on the reverse shock emission in a wider  $\sigma$ -range, as well as on various ejecta-medium interaction parameter regimes. We first (§ 2) present a rigorous analytical solution for the MHD  $90^\circ$  shock jump conditions, which is applicable for an arbitrary  $\sigma$ -value and for an arbitrary Lorentz factor  $\gamma_{21}$  between the upstream and the downstream. The detailed derivation and the relevant equations are presented in Appendix A. We then (§ 3) discuss the ejecta-medium interaction within the context of GRB fireball deceleration and reinvestigate the critical fireball radii and recategorize the thick versus thin shell regimes. This leads to a more complicated picture than in the pure hydrodynamical case (Sari & Piran 1995). In § 4, we calculate the synchrotron emission from the shocks under the conventional assumptions about the particle acceleration in collisionless shocks, and we present the predicted GRB early optical light curves for a wide range of  $\sigma$ -value. We discuss how the early afterglow data may be used to diagnose the magnetic content of GRB ejecta. Our results are summarized in § 5 with some discussions.

## 2. ANALYTICAL SOLUTION OF THE RELATIVISTIC $90^\circ$ SHOCKS

We now consider a relativistic shock that propagates into a magnetized medium. In the following analysis, the unshocked region (upstream) is denoted as region 1, the shocked region (downstream) is denoted as region 2, and the shock itself is

<sup>4</sup> If a GRB contains several well-separated emission episodes, the whole burst may even be separated into several discrete shells. In such cases, even a long-duration burst may be treated as the superposition of several thin shells rather than one single thick shell. See Zhang & Mészáros (2004) for more discussions.

denoted as “s.”<sup>5</sup> Hereafter,  $Q_{ij}$  denotes the value of the quantity  $Q$  in the region “i” in the rest frame of “j,” and  $Q_i$  denotes the value of the quantity  $Q$  in the region  $i$  in its own rest frame. For example,  $\gamma_{12}$  is the relative Lorentz factor between regions 1 and 2,  $\beta_{1s}$  is the relative velocity (in units of the speed of light  $c$ ) between region 1 and the shock, and  $B_{2s}$  is the magnetic field strength of region 2 in the rest frame of the shock, while  $B_1$  is the comoving magnetic field strength in region 1, etc. The relativistic  $90^\circ$  shock Rankine-Hugoniot relations could be written as (Kennel & Coroniti 1984)

$$n_1 u_{1s} = n_2 u_{2s}, \quad (1)$$

$$\mathcal{E} = \beta_{1s} B_{1s} = \beta_{2s} B_{2s}, \quad (2)$$

$$\gamma_{1s} \mu_1 + \frac{\mathcal{E} B_{1s}}{4\pi n_1 u_{1s}} = \gamma_{2s} \mu_2 + \frac{\mathcal{E} B_{2s}}{4\pi n_2 u_{2s}}, \quad (3)$$

$$\mu_1 u_{1s} + \frac{p_1}{n_1 u_{1s}} + \frac{B_{1s}^2}{8\pi n_1 u_{1s}} = \mu_2 u_{2s} + \frac{p_2}{n_2 u_{2s}} + \frac{B_{2s}^2}{8\pi n_2 u_{2s}}, \quad (4)$$

where  $\beta$  denotes the dimensionless velocity,  $\gamma = (1 - \beta^2)^{-1/2}$  denotes the Lorentz factor, and  $u = \beta\gamma$  denotes the radial four-velocity, so that  $\gamma^2 = 1 + u^2$ . Hereafter,  $n$ ,  $e$ , and  $p = (\hat{\Gamma} - 1)e$  denote the number density, internal energy, and thermal pressure, respectively, and  $\hat{\Gamma}$  is the adiabatic index. The enthalpy is  $nm_p c^2 + e + p$ , and the specific enthalpy can be written as

$$\mu = m_p c^2 + \frac{\hat{\Gamma}}{\hat{\Gamma} - 1} \frac{p}{n}, \quad (5)$$

where  $m_p$  is the proton mass and  $c$  is the speed of light. It is convenient to define a parameter

$$\sigma_i = \frac{B_i^2}{4\pi n_i \mu_i} = \frac{B_{is}^2}{4\pi n_i \mu_i \gamma_{is}^2} \quad (6)$$

to denote the degree of magnetization in each region. The magnetization parameter in the upstream region ( $\sigma_1$ ) is a more fundamental parameter, since it characterizes the magnetization of the flow itself. We therefore define<sup>6</sup>

$$\sigma \equiv \sigma_1 = \frac{B_{1s}^2}{4\pi n_1 \mu_1 \gamma_{1s}^2}. \quad (7)$$

In our problem, we are interested in a “cold” upstream flow, i.e.,  $e_1 = p_1 = 0$ , so that  $\mu_1 = m_p c^2$ . This is the only assumption made in the derivation. After some algebra (see Appendix A), we can finally write

$$\frac{e_2}{n_2 m_p c^2} = (\gamma_{21} - 1) \left[ 1 - \frac{\gamma_{21} + 1}{2u_{1s}(\gamma_{21}, \sigma) u_{2s}(\gamma_{21}, \sigma)} \sigma \right]. \quad (8)$$

Here  $u_{2s}(\gamma_{21}, \sigma)$  is a function of  $\gamma_{21}$  and  $\sigma$  and can be solved once  $\gamma_{21}$  and  $\sigma$  are known. After some analytical treatments of the relativistic Rankine-Hugoniot relations (eqs. [1]–[4]), one

can come up with an equation to solve  $u_{2s}$ . Since it is complicated, we only present it in Appendix A (eq. [A16]). Once  $u_{2s}$  is solved, we can also solve  $u_{1s}$  (using eq. [A8]), i.e.,

$$u_{1s}(\gamma_{21}, \sigma) = u_{2s}(\gamma_{21}, \sigma) \gamma_{21} + [u_{2s}^2(\gamma_{21}, \sigma) + 1]^{1/2} (\gamma_{21}^2 - 1)^{1/2}. \quad (9)$$

The compressive ratio can be derived directly from equation (1), i.e.,

$$\frac{n_2}{n_1} = \frac{u_{1s}(\gamma_{21}, \sigma)}{u_{2s}(\gamma_{21}, \sigma)} = \gamma_{21} + \frac{[u_{2s}^2(\gamma_{21}, \sigma) + 1]^{1/2}}{u_{2s}(\gamma_{21}, \sigma)} (\gamma_{21}^2 - 1)^{1/2}. \quad (10)$$

The main point here is that both  $e_2/n_2 m_p c^2$  and  $n_2/n_1$  can be determined by two unknown parameters, i.e.,  $\gamma_{21}$  and  $\sigma$ , so that when they are given arbitrarily, the whole problem is solved.

In the downstream region, the total pressure includes the contribution from the comoving thermal pressure  $p_2 = (\hat{\Gamma} - 1)e_2$  and the comoving magnetic pressure  $p_{b,2} = B_{2s}^2/8\pi$ . The ratio of the magnetic pressure to the thermal pressure is also a function of  $\sigma$  and  $\gamma_{21}$ :

$$\begin{aligned} \frac{p_{b,2}}{p_2} &= \left( \frac{\beta_{1s}}{\beta_{2s}} \right)^2 \frac{4\pi n_1 m_p c^2 \gamma_{1s}^2 \sigma}{8\pi \gamma_{2s}^2 (\hat{\Gamma} - 1) e_2} \\ &= \frac{1}{2(\hat{\Gamma} - 1)} \frac{u_{1s}}{u_{2s}} \sigma \left( \frac{e_2}{n_2 m_p c^2} \right)^{-1}, \end{aligned} \quad (11)$$

where equations (2) and (7) have been used.

The correctness of the solution (eq. [A16]) is verified in two asymptotic regimes.

### 2.1. The $\sigma = 0$ Regime

When  $\sigma = 0$ , the equation to solve  $u_{2s}^2(\gamma_{21}, \sigma)$  (eq. [A16]) is greatly simplified (eq. [A25]). All quantities can be expressed as a function of  $\gamma_{21}$ . The solutions are

$$u_{2s}^2 = \frac{(\gamma_{21} - 1)(\hat{\Gamma} - 1)^2}{\hat{\Gamma}(2 - \hat{\Gamma})(\gamma_{21} - 1) + 2}, \quad (12)$$

$$u_{1s}^2 = \frac{(\gamma_{21} - 1)(\hat{\Gamma}\gamma_{21} + 1)^2}{\hat{\Gamma}(2 - \hat{\Gamma})(\gamma_{21} - 1) + 2}, \quad (13)$$

$$\frac{e_2}{n_2} = (\gamma_{21} - 1) m_p c^2, \quad (14)$$

$$\frac{n_2}{n_1} = \frac{\hat{\Gamma}\gamma_{21} + 1}{\hat{\Gamma} - 1}, \quad (15)$$

$$\gamma_{1s}^2 = \frac{(\gamma_{21} + 1)[\hat{\Gamma}(\gamma_{21} - 1) + 1]^2}{\hat{\Gamma}(2 - \hat{\Gamma})(\gamma_{21} - 1) + 2}. \quad (16)$$

Equations (14)–(16) are just equations (3)–(5) of Blandford & McKee (1976), and they are the starting point for the hydrodynamical analysis of the reverse shock emission (e.g., Sari & Piran 1995). Under the limit of  $\gamma_{21} \gg 1$  and  $\hat{\Gamma} = 4/3$  (i.e., the downstream fluid is relativistic), equations (15) and (16) are reduced to the familiar forms of  $n_2/n_1 = 4\gamma_{21} + 3$ ,  $\gamma_{1s} \simeq \sqrt{2}\gamma_{21}$ , and  $\gamma_{2s} \simeq 3\sqrt{2}/4$  (or  $u_{2s} \simeq \sqrt{2}/4$ ).

<sup>5</sup> Note that such a notation system is only valid for § 2 and Appendix A. When discussing the GRB problem, i.e., the ejecta-medium interaction (§ 3), we introduce different meanings for the subscript numbers.

<sup>6</sup> Note that the definition is slightly different from that in Kennel & Coroniti (1984). We find that our definition allows the parameters to be coasted into an analytical form as a function of  $\sigma$  and  $\gamma_{21}$ .

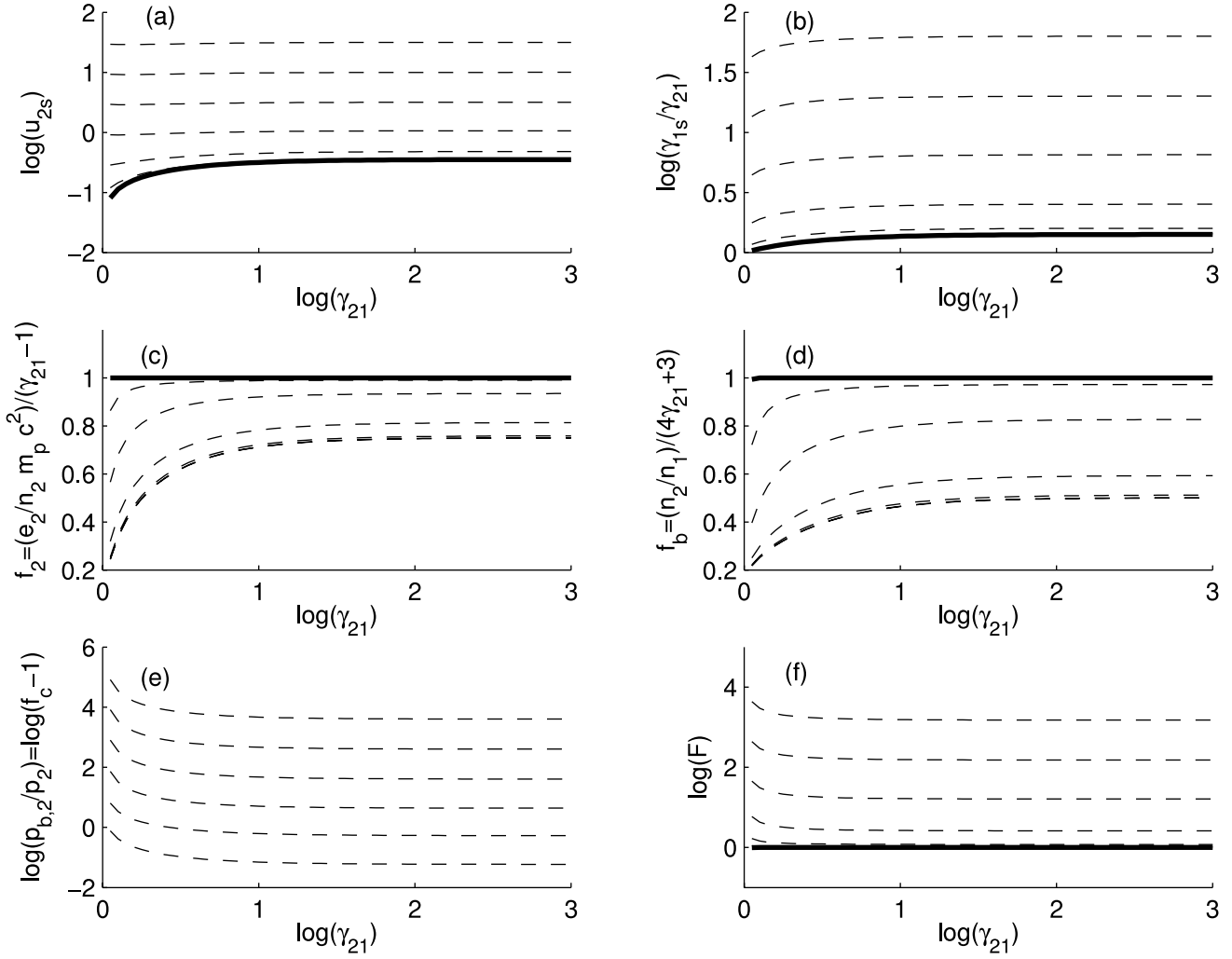


FIG. 1.—Variations of six parameters, i.e.,  $u_{2s}$ ,  $\gamma_{1s}/\gamma_{21}$ ,  $e_2/n_2 m_p c^2$ ,  $n_2/n_1$ ,  $p_{b,2}/p_2$ , and  $F$ , as a function of  $\gamma_{21}$ . The thick solid line indicates the case for  $\sigma = 0$ , which is the Blandford-McKee (1976) solution. For  $p_{b,2}/p_2$  (e), the  $\sigma = 0$  line is at negative infinity. The dashed lines, starting from the one closest to the thick line, are for  $\sigma = 0.01, 0.1, 1, 10, 100$ , and  $1000$ , respectively. The parameter  $e_2/n_2 m_p c^2$  (random Lorentz factor in the shocked, downstream region) is normalized to  $(\gamma_{21} - 1)$ , and the parameter  $n_2/n_1$  (compressive ratio) is normalized to  $(4\gamma_{21} + 3)$ ; both are the values expected in the  $\sigma = 0$  case.

## 2.2. The $\gamma_{21} \gg 1$ Regime

In the  $\gamma_{21} \rightarrow \infty$  limit, the equation for  $u_{2s}^2(\gamma_{21}, \sigma)$  (eq. [A16]) is also simplified (eq. [A26]). The solution of  $u_{2s}$  is a function of  $\sigma$  only, which reads

$$u_{2s}^2 = \frac{\hat{\Gamma}(1 - \hat{\Gamma}/4)\sigma^2 + (\hat{\Gamma}^2 - 2\hat{\Gamma} + 2)\sigma + (\hat{\Gamma} - 1)^2 + \sqrt{X}}{2\hat{\Gamma}(2 - \hat{\Gamma})(\sigma + 1)}, \quad (17)$$

where

$$\begin{aligned} X = & \hat{\Gamma}^2 \left(1 - \frac{\hat{\Gamma}}{4}\right)^2 \sigma^4 + \hat{\Gamma} \left(\frac{\hat{\Gamma}^3}{2} - 3\hat{\Gamma}^2 + 7\hat{\Gamma} - 4\right) \sigma^3 \\ & + \left(\frac{3}{2}\hat{\Gamma}^4 - 7\hat{\Gamma}^3 + \frac{31}{2}\hat{\Gamma}^2 - 14\hat{\Gamma} + 4\right) \sigma^2 \\ & + 2(\hat{\Gamma} - 1)^2(\hat{\Gamma}^2 - 2\hat{\Gamma} + 2)\sigma + (\hat{\Gamma} - 1)^4. \end{aligned} \quad (18)$$

Notice that there are two solutions with the term  $\pm\sqrt{X}$  in the numerator of equation (17), but the minus term leads to negative

pressure and is unphysical. For a relativistic downstream region, i.e.,  $\hat{\Gamma} = 4/3$ , the solution is reduced to

$$\begin{aligned} u_{2s}^2 &= \frac{8\sigma^2 + 10\sigma + 1 + \sqrt{64\sigma^2(\sigma + 1)^2 + 20\sigma(\sigma + 1) + 1}}{16(\sigma + 1)} \\ &= \frac{8\sigma^2 + 10\sigma + 1 + (2\sigma + 1)\sqrt{16\sigma^2 + 16\sigma + 1}}{16(\sigma + 1)}. \end{aligned} \quad (19)$$

This is equation (4.11) of Kennel & Coroniti (1984). With  $u_{2s}$ , one can derive  $u_{1s}$  using equation (9), which depends on  $\gamma_{21}$  as well. The quantities  $e_2/n_2 m_p c^2$  and  $n_2/n_1$  can also be derived accordingly. In the  $\sigma = 0$  limit, equation (19) is reduced to  $u_{2s} \simeq \sqrt{2}/4$ , which is consistent with the asymptotic results in § 2.1.

## 2.3. The General Cases

For more general cases with arbitrary values of  $\gamma_{21}$  and  $\sigma$ ,  $u_{2s}^2(\gamma_{21}, \sigma)$  has to be solved rigorously. The equation (eq. [A16]) is solved numerically, and the solutions indeed show deviations from both asymptotic regimes for arbitrary  $\gamma_{21}$  and  $\sigma$ -values.

Figure 1 shows the variations of six parameters, i.e.,  $u_{2s}$ ,  $\gamma_{1s}/\gamma_{21}$ ,  $e_2/n_2 m_p c^2$ ,  $n_2/n_1$ ,  $p_{b,2}/p_2$ , and  $F$  (see definition in eq. [33])

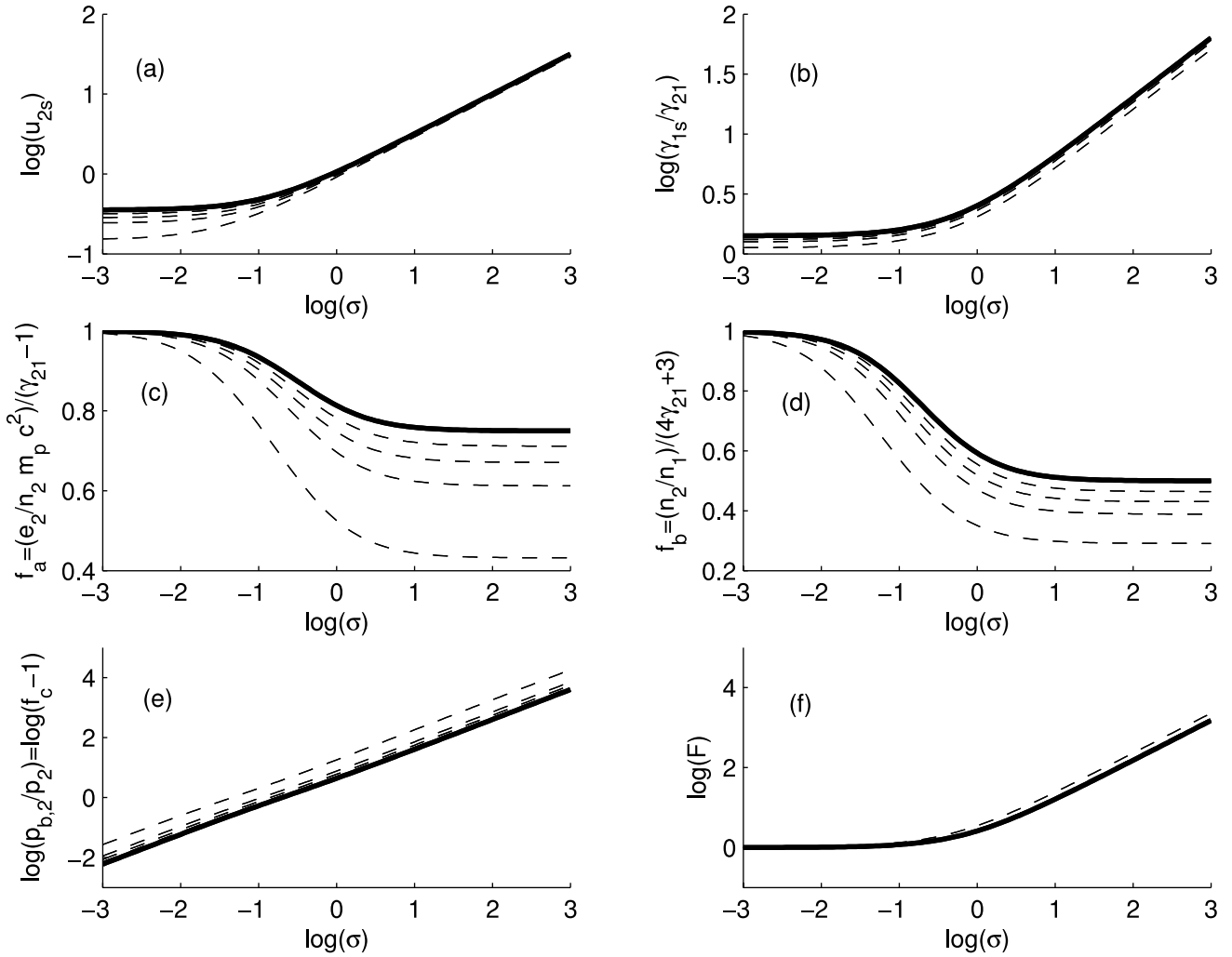


FIG. 2.—Variations of six parameters, i.e.,  $u_{2s}$ ,  $\gamma_{1s}/\gamma_{21}$ ,  $e_2/n_2 m_p c^2$ ,  $n_2/n_1$ ,  $p_{b,2}/p_2$ , and  $F$ , as a function of  $\sigma$ . The thick solid line is the Kennel-Coroniti (1984) solution, denoting a  $\gamma_{21} \gg 1$  regime. The dashed lines, starting from the one closest to the thick line, are for  $\gamma_{21} = 1000, 100, 10, 5, 3$ , and  $1.5$ , respectively. Again the parameters  $e_2/n_2 m_p c^2$  and  $n_2/n_1$  are normalized to  $(\gamma_{21} - 1)$  and  $(4\gamma_{21} + 3)$ , respectively.

as a function of  $\gamma_{21}$ . The thick solid line indicates the case for  $\sigma = 0$ , which is the strict Blandford-McKee (1976) regime. The dashed lines, starting from the one closest to the thick line, are for  $\sigma = 0.01, 0.1, 1, 10, 100$ , and  $1000$ , respectively. In order to find out the correction factors to the pure hydrodynamical case, we normalize  $e_2/n_2 m_p c^2$  and  $n_2/n_1$  with respect to the  $\sigma = 0$  case.  $\hat{\Gamma} = 4/3$  has been adopted. We find that all the parameters achieve asymptotic values when  $\gamma_{21} \gg 1$  and that the asymptotic value depends on the value of  $\sigma$ . In Figure 2 we plot the variations of the same six parameters as a function of  $\sigma$ . The thick solid line is the  $\gamma_{21} \gg 1$  Kennel-Coroniti (1984) limit, and the dashed lines, starting from that closest to the thick line, correspond to  $\gamma_{21} = 1000, 100, 10, 5, 3$ , and  $1.5$ , respectively. For  $\gamma_{21} > 100$ , the Kennel-Coroniti approximation is good enough.

An obvious conclusion from Figures 1 and 2 is that all the (normalized) parameters are insensitive to  $\gamma_{21}$  (especially when  $\gamma_{21}$  is greater than a few) but are sensitive to  $\sigma$ . Both  $u_{2s}$  and  $\gamma_{1s}/\gamma_{21}$  increase with  $\sigma$ , while both  $e_2/n_2 m_p c^2$  and  $n_2/n_1$  decrease with  $\sigma$ . For  $\gamma_{1s}/\gamma_{21}$ , as long as  $\gamma_{21}$  is mildly large (e.g.,  $>3$ ), the ratio is essentially a function of  $\sigma$  only. It starts from the conventional value  $\sqrt{2}$  in the  $\sigma \sim 0$  regime and increases quickly as  $\sigma$  approaches unity, which means that the shock leads the fluid substantially (in the upstream rest frame) in the high- $\sigma$  regime. Both  $e_2/n_2 m_p c^2$  and  $n_2/n_1$  are suppressed when  $\sigma$  increases, but

the suppression factor (with respect to the  $\sigma = 0$  limit) is not large, especially when  $\gamma_{21}$  is not too small. For example, for  $\gamma_{21} > 3$ , the suppression factor for  $e_2/n_2$  is larger than  $0.6$ , while that for  $n_2/n_1$  is larger than  $0.4$ . Furthermore, the suppression factor reaches an asymptotic value when  $\sigma$  approaches several. This result is very interesting, since conventionally it is believed that the shock is completely suppressed when  $\sigma$  reaches larger values. Our results suggest that *relativistic strong shocks still exist in the high- $\sigma$  regime*. The suppression factor, which essentially does not depend on  $\sigma$ , is only mild as long as the shock is relativistic. The overall efficiency of converting the total energy (the kinetic energy plus the Poynting flux energy) to heat still decreases steadily with increasing  $\sigma$ . The reason is not that the shock (which converts the kinetic energy into heat) itself is less strong but rather that the fraction of the kinetic energy in the total energy, i.e.,  $(1 + \sigma)^{-1}$ , becomes smaller as  $\sigma$  becomes larger.

### 3. EJECTA-MEDIUM INTERACTION

#### 3.1. Basic Equations

Now we consider an arbitrarily magnetized flow with magnetization parameter  $\sigma$  and Lorentz factor  $\gamma = \gamma_4$  being decelerated by an ambient medium with density  $n = n_1$ . A pair of shocks form when the shock-forming condition is satisfied, i.e.,

the relative velocity between the two colliders exceeds the sound velocity in the medium and the magnetoacoustic wave velocity of the ejecta, and the pressure in the shocked region exceeds the pressure in the unshocked region. In the GRB case (a relativistic ejecta), a forward shock always forms, while a reverse shock may not always form if  $\sigma$  is too large. In the high- $\sigma$  regime, the magnetoacoustic wave velocity is essentially the Alfvén velocity for a  $90^\circ$  shock. The first condition for the reverse shock formation is  $\gamma_{41} \gg \gamma_A \sim (1 + \sigma)^{1/2}$ , where  $\gamma_A$  is the Alfvén Lorentz factor in the ejecta. For GRBs we have  $\gamma_{41} \geq 100$  (to ensure that the observed gamma-ray spectrum is nonthermal), so this condition is satisfied as long as  $\sigma \leq 10^4$ . The second condition is generally more stringent, which is expressed in equations (31) and (43) below. In any case, with reasonable parameters a reverse shock could be formed when  $\sigma$  is less than hundreds or tens. When the reverse shock forms, we can then investigate a picture where two shocks and one contact discontinuity separate the ejecta and medium into four regions. Below we take the usual convention to define the four regions: (1) unshocked medium, (2) shocked medium, (3) shocked ejecta, and (4) unshocked ejecta. Notice that hereafter the numerical subscripts have different meanings from the ones used in § 2 and the Appendix, where the numbers “1” and “2” denote upstream and downstream, respectively. For the forward shock, both sets of notations coincide, while for the reverse shock, the previous “1” and “2” are replaced by “4” and “3,” respectively. We assume that the ambient medium is not magnetized so that  $\sigma_1 = 0$ , but we assign an arbitrary magnetization parameter

$$\sigma \equiv \sigma_4 = \frac{B_4^2}{4\pi n_4 m_p c^2} = \frac{B_{4s}^2}{4\pi n_4 m_p c^2 \gamma_{4s}^2} \quad (20)$$

for the ejecta. Since we are discussing the problem in the rest frame of the medium, we drop out the subscript “1” whenever it means “in the rest frame of region 1.” We can then write the following relations based on the shock jump conditions. Throughout the following discussions,  $\hat{\Gamma} = 4/3$  is adopted.

$$\frac{e_2}{n_2 m_p c^2} = (\gamma_2 - 1) \simeq \gamma_2, \quad (21)$$

$$\frac{n_2}{n_1} = 4\gamma_2 + 3 \simeq 4\gamma_2, \quad (22)$$

$$\frac{e_3}{n_3 m_p c^2} = (\gamma_{34} - 1) f_a, \quad (23)$$

$$\frac{n_3}{n_4} = (4\gamma_{34} + 3) f_b, \quad (24)$$

where

$$f_a = f_a(\sigma, \gamma_{34}) = 1 - \frac{\gamma_{34} + 1}{2[u_{3s}^2 \gamma_{34} + u_{3s}(u_{3s}^2 + 1)^{1/2}(\gamma_{34}^2 - 1)^{1/2}]} \sigma \quad (25)$$

and

$$f_b = f_b(\sigma, \gamma_{34}) = \frac{\gamma_{34} + [(u_{3s}^2 + 1)^{1/2}/u_{3s}](\gamma_{34}^2 - 1)^{1/2}}{4\gamma_{43} + 3} \quad (26)$$

are the correction factors for  $e_3/n_3 m_p c^2$  and  $n_3/n_4$  with respect to the  $\sigma = 0$  limit, and  $u_{3s}$  is a function of  $\gamma_{34}$  and  $\sigma$ , whose solution is found in Appendix A (eq. [A16]). The functions  $f_a$  and  $f_b$  are plotted as a function of  $\sigma$  in Figures 2c and 2d, respectively,

which show  $f_a \rightarrow 1$  and  $f_b \rightarrow 1$  when  $\sigma \rightarrow 0$ . Constant speed across the contact discontinuity gives

$$\gamma_2 = \gamma_3, \quad (27)$$

and constant pressure across the contact discontinuity gives

$$\frac{e_2}{3} = \frac{e_3}{3} + \frac{B_3^2}{8\pi} = \frac{e_3}{3} \left(1 + \frac{p_{b,3}}{p_3}\right), \quad (28)$$

or

$$e_2 = e_3 f_c, \quad (29)$$

where

$$f_c = f_c(\sigma, \gamma_{34}) = 1 + \frac{p_{b,3}}{p_3} \quad (\propto \sigma). \quad (30)$$

The pressure ratio  $p_{b,3}/p_3$  is calculated according to equation (11), whose dependence on  $\sigma$  is plotted in Figure 2e, which shows a  $\propto \sigma$  dependence in the  $\sigma \gg 1$  asymptotic regime. Hereafter we indicate the asymptotic behavior in the  $\sigma \gg 1$  limit in a pair of parentheses immediately following an equation.

In order to have equation (29) satisfied, the condition should be that the thermal pressure generated in the forward shock is stronger than the magnetic pressure in region 4. This gives  $B_4^2/8\pi < (4/3)\gamma_4^2 n_1 m_p c^2$ . Noticing equation (20), the condition for the existence of the reverse shock can be written as

$$\sigma < \frac{8}{3} \gamma_4^2 \frac{n_1}{n_4}. \quad (31)$$

When the reverse shock exists, using equations (21)–(24) and (29), one can finally get

$$\frac{n_4}{n_1} F = \frac{(\gamma_2 - 1)(4\gamma_2 + 3)}{(\gamma_{34} - 1)(4\gamma_{34} + 3)}, \quad (32)$$

where

$$F = f_a f_b f_c, \quad (33)$$

with  $f_a$ ,  $f_b$ , and  $f_c$  defined in equations (25), (26), and (30), respectively. The parameter  $F$  has been calculated for different input parameters, and the results are shown in Figures 1f and 2f. We can see that  $F$  is very insensitive to  $\gamma_{34}$  and is essentially a function of  $\sigma$  only. The asymptotic behavior in the  $\sigma \gg 1$  regime is  $F(\sigma) \propto \sigma$ . We then write

$$F(\gamma_{34}, \sigma) \simeq F(\sigma) \quad (\propto \sigma). \quad (34)$$

Equation (32) can be used to define whether the reverse shocks upstream and downstream are relativistic with respect to each other. Similar to the analysis of Sari & Piran (1995), we analyze the value of  $(n_4/n_1)F/\gamma_4^2$ . The relative Lorentz factor of the reverse shocks upstream and downstream is

$$\gamma_{34} \simeq \frac{1}{2} \left( \frac{\gamma_4}{\gamma_3} + \frac{\gamma_3}{\gamma_4} \right). \quad (35)$$

For the relativistic case, i.e.,  $\gamma_{34} \gg 1$ , we have  $(n_4/n_1)F/\gamma_4^2 \sim \gamma_2^2/(\gamma_{34}^2 \gamma_4^2) \sim \gamma_2^2/\gamma_4^2 \ll 1$ . On the other hand, for a nonrelativistic case, we have  $\gamma_{34} \sim 1$ ,  $\gamma_4 \sim \gamma_3$ , and  $(\gamma_{34} - 1)(4\gamma_{34} + 3) = \epsilon \ll 1$ . This gives  $(n_4/n_1)F/\gamma_4^2 \sim 1/\epsilon \gg 1$ . We thus conclude that the reverse shock upstream is relativistic with respect to the

downstream when  $\gamma_4^2 \gg (n_4/n_1)F$ , while it is nonrelativistic when  $\gamma_4^2 \ll (n_4/n_1)F$ . For  $\sigma = 0$ , we have  $F = 1$ , and the result is fully consistent with Sari & Piran (1995).

### 3.2. Critical Radii

We consider an isotropic fireball with total energy  $E = E_K + E_P$ , where  $E_K$  is the kinetic energy and  $E_P$  is the Poynting flux energy. The discussions are also valid for a collimated jet by regarding the various energy components as the ‘‘isotropic’’ values. With the definition of  $\sigma$  (eq. [7]), we find  $E_P/E_K \sim \sigma$  (from eq. [4]),<sup>7</sup> so that  $E = E_K(1 + \sigma)$ , or  $E_K = E/(1 + \sigma)$  (see also Zhang & Mészáros 2002). We follow the traditional convention of defining the Sedov length  $l \sim (E/n_1 m_p c^2)^{1/3}$ , where the total energy is adopted. The shell baryon number density  $n_4$  is, however, defined by  $E_K$ . The density ratio is  $n_4/n_1 \sim l^3/[\gamma_4^2 \Delta R^2(1 + \sigma)]$ , where  $\Delta = \max(\Delta_0, R/\gamma_4^2)$  is the thickness of the shell,  $\Delta_0 = cT$  is the initial width of the shell, and  $R$  is the fireball radius. This holds for both a nonspreading shell (where  $\Delta = \Delta_0$  is a constant) and for a spreading shell (where  $\Delta \sim R/\gamma_4^2$ ).

Below we revisit the four critical radii related to the reverse shock deceleration (Sari & Piran 1995). In our following discussion, we assume that a reverse shock exists. The asymptotic behaviors at  $\sigma \gg 1$  for various correction factors (presented in parentheses) therefore are valid for the  $\sigma$ -range in which the reverse shock-forming condition is satisfied.

1. The fireball radius for the relative Lorentz factor between the reverse shocks upstream and downstream (i.e.,  $\gamma_{34}$ ) to transform from the Newtonian regime to the relativistic regime can be estimated according to  $\gamma_4^2 \sim (n_4/n_1)F$ , which gives

$$R_N \sim \frac{l^{3/2}}{\Delta^{1/2} \gamma_4^2} C_N, \quad (36)$$

where

$$C_N(\gamma_{34}, \sigma) \simeq C_N(\sigma) = \left[ \frac{F(\sigma)}{1 + \sigma} \right]^{1/2} \sim 1 \quad (\propto \sigma^0) \quad (37)$$

is the correction factor of  $R_N$  with respect to the  $\sigma = 0$  case. Since both  $F(\sigma)$  and  $(1 + \sigma)$  have the same asymptotic behavior ( $\propto \sigma$ ) at high  $\sigma$ , the final correction factor  $C_N$  is always of order unity throughout (see Fig. 3), and we neglect it in the following discussions.

2. The radius where the reverse shock crosses the shell is approximately (Sari & Piran 1995)  $R_\Delta = [\Delta/(\beta_4 - \beta_2)][1 - (\gamma_4/\gamma_3)(n_4/n_3)]$ . In the  $\sigma = 0$  case, the factor  $[1 - (\gamma_4/\gamma_3)(n_4/n_3)]$ , which delineates the relative compression factor due to shock crossing,<sup>8</sup> is a factor ranging from  $\frac{1}{2}$  to  $\frac{6}{7}$ , which was neglected for order-of-magnitude estimates (Sari & Piran 1995). For arbitrary  $\sigma$ -values, this parameter is  $\sigma$ -sensitive (through the dependence of  $f_b(\sigma)$ ; see eq. [26]), i.e., becomes  $\ll 1$  when  $\sigma \gg 1$ , so we cannot drop it out. Following a procedure similar to that of Sari

<sup>7</sup> The full presentation of eq. [4] should be  $\mu_1 u_{1s} + p_1/n_1 u_{1s} + B_{1s}^2/8\pi n_1 u_{1s} + B_{1s}^2 \beta_{1s}^2/8\pi n_1 u_{1s} = \mu_2 u_{2s} + p_2/n_2 u_{2s} + B_{2s}^2/8\pi n_2 u_{2s} + B_{2s}^2 \beta_{2s}^2/8\pi n_2 u_{2s}$ . So strictly speaking,  $E_P/E_K = \sigma(1 + \beta_{1s}^2)/2\beta_{1s}^2$ . In the high- $\sigma$  regime, we have  $\beta_{1s} \sim 1$  and the factor  $(1 + \beta_{1s}^2)/2\beta_{1s}^2 \simeq 1$ . In the low- $\sigma$  regime,  $\beta_{1s} < 1$ , but the factor  $[1 + \sigma(1 + \beta_{1s}^2)/2\beta_{1s}^2]$  is in any case  $\sim 1$ . We therefore neglect the  $(1 + \beta_{1s}^2)/2\beta_{1s}^2$  factor in the following discussion.

<sup>8</sup> If one assumes that after shock crossing a shell with width  $\Delta$  becomes  $\Delta'$ , this parameter is simply  $(\Delta - \Delta')/\Delta$ .

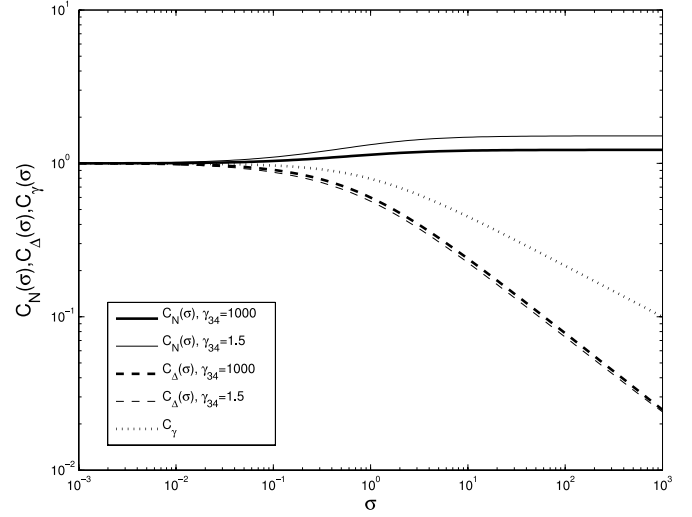


FIG. 3.—Functions  $C_N(\sigma)$ ,  $C_\Delta(\sigma)$ , and  $C_\gamma$  calculated for both  $\gamma_{34} = 1.5$  and  $\gamma_{34} = 1000$ .

& Piran (1995) and replacing  $n_4/n_1$  (in the  $\sigma = 0$  case) with  $(n_4/n_1)F$ , one finally has

$$R_\Delta \sim \gamma_4 \Delta \left[ \frac{n_4}{n_1} F(\sigma) \right]^{1/2} \left( 1 - \frac{\gamma_4 n_4}{\gamma_3 n_3} \right) \sim \Delta^{1/4} l^{3/4} C_\Delta, \quad (38)$$

where

$$\begin{aligned} C_\Delta(\gamma_{34}, \sigma) &\simeq C_\Delta(\sigma) = \left[ \frac{F(\sigma)}{1 + \sigma} \right]^{1/4} \left( 1 - \frac{\gamma_4 n_4}{\gamma_3 n_3} \right)^{1/2} \\ &\sim \left( 1 - \frac{\gamma_4 n_4}{\gamma_3 n_3} \right)^{1/2} (\propto \sigma^{-1/2}) \end{aligned} \quad (39)$$

is the correction factor of  $R_\Delta$  with respect to the  $\sigma = 0$  case. This correction factor suggests that the reverse shock crosses the shell faster when  $\sigma$  becomes larger.

3. The conventional ‘‘deceleration radius’’ (for the thin shell case) is modified in the high- $\sigma$  regime. According to equation (2), the ratio of the comoving magnetic fields in regions 4 and 3 is  $B_4/B_3 = u_{3s}/u_{4s}$ . The lab frame ratio of the Poynting flux energy in both regions can be written as

$$\frac{E_{P,4}}{E_{P,3}} = \frac{\gamma_4 (B_4^2/n_4)}{\gamma_3 (B_3^2/n_3)} = \frac{u_{3s} \gamma_4}{u_{4s} \gamma_3} \sim 1, \quad (40)$$

where ‘‘ $\sim$ ’’ applies in the  $\sigma \gg 1$  limit so that  $u_{4s} \sim \gamma_{4s}$  and  $u_{3s} \sim \gamma_{3s}$ . Since  $\gamma_{4s}/\gamma_{3s} = \gamma_4/\gamma_3$  (both have the same relation with  $\gamma_{34}$ ; eq. [35]), equation (40) is naturally derived. We have calculated this ratio numerically and found that in the high- $\sigma$  limit, the difference between this ratio and unity is a small quantity comparing  $\sigma^{-1}$ . This manifests that shocks in the high- $\sigma$  limit only effectively dissipate the kinetic energy (in the baryonic component) in the upstream, and the Poynting energy (in the lab frame) essentially remains the same. As a result, one should define the deceleration radius (for the thin shell case) using  $E_K$  alone, so that

$$R_\gamma \sim \frac{l}{\gamma_4^{2/3} (1 + \sigma)^{1/3}} \sim \frac{l}{\gamma_4^{2/3}} C_\gamma, \quad (41)$$

where

$$C_\gamma(\sigma) = (1 + \sigma)^{-1/3} \quad (\propto \sigma^{-1/3}). \quad (42)$$

Notice that the radius  $R_\gamma$  is still the radius where the fireball collects  $1/\gamma_4$  of the fireball rest mass.<sup>9</sup>

In the above discussion, we have already assumed that a reverse shock exists. In order to satisfy condition (31) at  $R_\gamma$ , one can put a more explicit constraint on  $\sigma$ , which reads

$$\sigma < 100 \left( \frac{\gamma_4}{300} \right)^4 \left( \frac{T}{10 \text{ s}} \right)^{3/2} \left( \frac{E}{10^{52} \text{ ergs}} \right)^{-1/2}. \quad (43)$$

We can see that for typical GRB parameters, a reverse shock exists when  $\sigma$  is smaller than several tens to several hundreds.

It is worth noting that at the deceleration radius, the Poynting energy is not yet transferred to the ISM. At the end shock crossing, the magnetic pressure behind the contact discontinuity balances the thermal pressure in the forward shock crossing. It is not until the fireball decelerates that the bulk of the magnetic energy in the ejecta transfers to the forward shock region. During the deceleration, the magnetic fields push the contact discontinuity from behind and transfer energy through  $pdV$  work. Eventually, the total energy will be transferred to the ISM, so the late-time afterglow level is still defined by the total energy of the fireball. The detailed energy transfer process is complicated and will be studied carefully in a future work (see Zhang & Kobayashi 2005 for a brief discussion). This point is relevant to the calculations of the forward shock emission level, and it is further discussed in § 4.4.

In Figure 3 we numerically plot the functions  $C_N(\sigma)$ ,  $C_\Delta(\sigma)$ , and  $C_\gamma(\sigma)$  for both the mildly relativistic case ( $\gamma_{34} = 1.5$ ) and the extremely relativistic case ( $\gamma_{34} = 1000$ ). We can see that  $C_N$  is insensitive to both  $\gamma_{34}$  and  $\sigma$ , and we treat it as a constant of order unity. The correction factor  $C_\Delta$  is rather insensitive to  $\gamma_{34}$  and is essentially a function of  $\sigma$  only. In the  $\sigma \gg 1$  regime, we have  $C_\Delta \propto \sigma^{-1/2}$ . By definition,  $C_\gamma$  is a function of  $\sigma$  only.

4. Finally, the radius where the shell spreads is still defined by

$$R_s \sim \gamma_4^2 \Delta_0. \quad (44)$$

Taking the convention of defining (Sari & Piran 1995)

$$\xi \equiv \frac{(l/\Delta)^{1/2}}{\gamma_4^{4/3}}, \quad (45)$$

one has the following equation:

$$\frac{R_N}{\xi} = \frac{R_\gamma}{C_\gamma} = \frac{\xi^{1/2}}{C_\Delta} R_\Delta = \xi_0^2 R_s, \quad (46)$$

<sup>9</sup> This could be derived using an energy conservation equation in the lab frame before and after the shock crossing(s), i.e.,  $\gamma_4(M_0 c^2 + U_{B,0}) + M_{\text{ISM}} c^2 = \gamma_2(M_0 c^2 + \gamma_2 M_{\text{ISM}} c^2 + U_B)$ , where  $M_0$  is the mass in the original ejecta,  $M_{\text{ISM}}$  is the collected ISM mass as the reverse shock crosses the shell,  $U_{B,0}$  is the initial comoving magnetic energy, and  $U_B$  is the comoving magnetic energy after shock crossing. This gives  $(\gamma_4 - \gamma_2)M_0 c^2 + (E_{P,4} - E_{P,3}) = (\gamma_2^2 - 1)M_{\text{ISM}} c^2$ , where  $E_{P,4} = \gamma_4 U_{B,0}$  and  $E_{P,3} = \gamma_2 U_B$ . According to equation (40), the term  $(E_{P,4} - E_{P,3})$  drops out from the energy conservation equation, so the equation is effectively the familiar hydrodynamical one with the total energy being  $E_K = E/(1 + \sigma)$ .

where

$$\xi_0 \equiv \frac{(l/\Delta_0)^{1/2}}{\gamma_4^{4/3}} = \left( \frac{t_\gamma}{T} \right)^{1/2} \quad (47)$$

is the  $\xi$ -value for  $R \leq R_s$  (i.e., no spreading occurs), where

$$t_\gamma \equiv \frac{R_\gamma}{C_\gamma \gamma_4^2 c} \sim \frac{l}{\gamma_4^{8/3} c}. \quad (48)$$

Note that this notation is exactly the same as in the  $\sigma = 0$  case, and the total energy  $E$  is used (in defining  $l$ ). This makes  $t_\gamma$  a constant not depending on  $\sigma$ , which is convenient for the discussions of the various parameter regions in the next section.

### 3.3. Parameter Regions: Thick vs. Thin Shell Regimes

Equating the four critical radii defines six critical lines in the  $\xi_0$ - $\sigma$  or the  $T/t_\gamma$ - $\sigma$  space. This is justified by the fact that the spreading regime [which makes  $\xi$  deviate from  $\xi_0 = (t_\gamma/T)^{1/2}$ ] always happens below the critical lines and, hence, does not influence the location of the critical lines. The six critical lines are

$$\begin{aligned} R_\gamma \sim R_\Delta, \quad \frac{T}{t_\gamma} &\sim \left( \frac{C_\gamma}{C_\Delta} \right)^4 \sim Q \quad (\propto \sigma^{2/3}); \\ R_N \sim R_\Delta, \quad \frac{T}{t_\gamma} &\sim C_\Delta^{-4/3} \sim Q \quad (\propto \sigma^{2/3}); \\ R_N \sim R_\gamma, \quad \frac{T}{t_\gamma} &\sim C_\gamma^{-2} \sim Q \quad (\propto \sigma^{2/3}); \\ R_N \sim R_s, \quad \frac{T}{t_\gamma} &\sim 1 \quad (\propto \sigma^0); \\ R_\gamma \sim R_s, \quad \frac{T}{t_\gamma} &\sim C_\gamma \sim Q^{-1/2} \quad (\propto \sigma^{-1/3}); \\ R_\Delta \sim R_s, \quad \frac{T}{t_\gamma} &\sim C_\Delta^{4/3} \sim Q^{-1} \quad (\propto \sigma^{-2/3}). \end{aligned} \quad (49)$$

We can see that the first three lines have the same asymptotic behavior at high  $\sigma$ , and calculations show that they essentially coincide with each other. Hereafter, we define

$$Q(\sigma) \equiv [C_\gamma(\sigma)]^{-2} \sim C_\Delta^{-4/3} \sim \left( \frac{C_\gamma}{C_\Delta} \right)^4 \quad (\propto \sigma^{2/3}), \quad (50)$$

so that  $C_\Delta \sim Q^{-3/4}$  and  $C_\gamma \sim Q^{-1/2}$ , and equation (46) can be rewritten as

$$\frac{R_N}{\xi} = Q^{1/2} R_\gamma = \xi^{1/2} Q^{3/4} R_\Delta = \xi_0^2 R_s. \quad (51)$$

In principle, changing the order between  $R_N$  and  $R_s$  and between  $R_\gamma$  and  $R_s$  does not lead to essential modifications of the shock crossing and deceleration physics, so that the fourth and fifth lines in equation (49) are not crucial. We therefore essentially have two lines that separate three physical regimes in  $T/t_\gamma$ - $\sigma$  space (Fig. 4).

*Region I.*—The thick shell regime. This is the region where  $T/t_\gamma > Q$  is satisfied. In this region, one has  $R_N < R_\gamma < R_\Delta < R_s$ . The downstream becomes relativistic with respect to the upstream before the reverse shock crosses the shell (Sari & Piran 1995). The full deceleration occurs at the end of shock crossing,

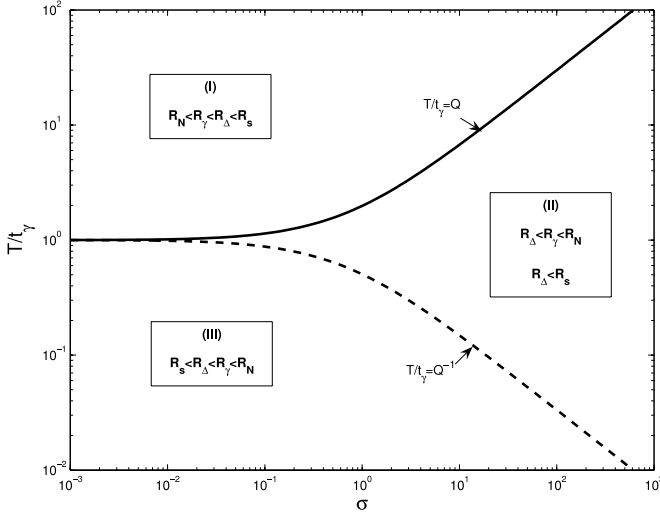


FIG. 4.—Parameter regimes in the  $(T/t_\gamma)$ – $\sigma$  space.

i.e., at  $R \sim R_\Delta$  (Kobayashi et al. 1999). Given a certain observed central engine activity time  $T$ , a total energy  $E$ , and an ambient density  $n$ , one can also define a critical Lorentz factor

$$\gamma_c \simeq 125 E_{52}^{1/8} n^{-1/8} T_2^{-3/8} Q^{3/8} \left( \frac{1+z}{2} \right)^{3/8}, \quad (52)$$

where some refined coefficients and the cosmological time dilation factor are explicitly taken into account in order to get the numerical value (here  $z$  is the GRB redshift). For  $\gamma_0 > \gamma_c$ , one is in the thick shell regime, while for  $\gamma_0 < \gamma_c$ , one is in the thin shell regime. The function  $Q(\sigma)$  is plotted as the top curve in Figure 4. In the  $\sigma \ll 1$  regime,  $Q(\sigma) \sim 1$ . For  $\sigma \gg 1$ , we have  $Q(\sigma) \propto \sigma^{2/3}$ , and hence  $\gamma_c \propto \sigma^{1/4}$ . We can see that given the same values for the other parameters, the parameter space for the thick shell regime is greatly reduced when  $\sigma$  is high. More bursts are in the thin shell regime.

*Region II.*—The nonspreaing thin shell regime. This region is defined by  $Q^{-1} < T/t_\gamma < Q$ , in which  $R_\Delta < R_\gamma < R_N$  and  $R_\Delta < R_s$  are satisfied. The common features of this regime are that the reverse shock crosses the shell (at  $R_\Delta$ ) before noticeable deceleration occurs (at  $R_\gamma$ ; e.g., the Lorentz factor is reduced by roughly a factor of 2), that the relative speed between the upstream and the downstream never becomes relativistic, and that the shell does not spread during the first shock crossing. The separation between  $R_\Delta$  and  $R_\gamma$  leads to some novel features for the reverse shock emission. During the first shock crossing the shell is heated so that electrons start to emit. However, after the first shock crossing, the shell is not decelerated significantly. It is difficult to delineate the detailed process at this stage, but a rough picture is that higher order shocks may form and bounce back and forth between the inner edge of the shell and the contact discontinuity. This happens until the shell reaches  $R_\gamma$ . It is likely that the shell remains heated by the multicrossing of shocks and electrons keep radiating at a high level for an extended period of time. One then expects a broad reverse shock emission peak, which is a novel phenomenon in the high- $\sigma$  thin shell regime. Notice that when  $\sigma$  is very large, a reverse shock may not form at  $R_\Delta$  at all. However, since  $R_\Delta$  is the smallest in the problem, whenever a reverse shock forms, it quickly crosses the shell in a radius of  $R_\Delta$ , and the above discussion is still valid.

*Region III.*—The spreading thin shell region. This is defined by  $T/t_\gamma < Q^{-1}$ , in which  $R_s < R_\Delta < R_\gamma < R_N$  is satisfied. Since

$R_\Delta < R_\gamma$ , again multicrossing of shocks is needed to slow down the ejecta, and the downstream never becomes relativistic with respect to the upstream. The novel feature in this region compared with region II is that the shell starts to spread before shock crossing, so the three radii have the relationship

$$C_\gamma^{2/3} R_N = R_\gamma = \left( \frac{C_\gamma}{C_\Delta} \right)^2 R_\Delta, \quad (53)$$

or

$$Q^{-1/3} R_N \simeq R_\gamma \simeq Q^{1/2} R_\Delta. \quad (54)$$

We can see that the triple coincidence  $R_N = R_\gamma = R_\Delta$  in the thin shell regime (Sari & Piran 1995) is only valid when  $\sigma$  is small. According to Figure 4, this practically happens when  $\sigma \leq 0.01$ .

### 3.4. Critical Times

We finally derive the shock crossing time  $t_\times$  and the deceleration time  $t_{\text{dec}}$  as measured by the observer. In the literature, to study the  $\sigma = 0$  regime,  $t_{\text{dec}} = t_\times \sim R_\Delta / \gamma_2^2 c \sim \max(T, t_\gamma C_\gamma) \sim \max(T, t_\gamma)$  has conventionally been adopted (noting that  $C_\gamma = 1$  when  $\sigma = 0$ ). When an arbitrary  $\sigma$ -value is adopted, there are further complications to quantifying these critical times. First, although in the thick shell regime (I)  $t_{\text{dec}} = t_\times$  is still valid, in the thin shell regimes (II and III) the deceleration radius  $R_\gamma$  is larger than the shock crossing radius  $R_\Delta$ , so  $t_\times < t_{\text{dec}}$ . Second, the timescale  $R_\Delta / \gamma_2^2 c$  only describes the delay timescales for the emission coming from the radius  $R_\Delta$  with respect to the emission from the internal shock radius, for an infinitely thin shell. A more precise description of the reverse shock emission peak time should include the thickness of the radiation region. The real shock crossing time should correspond to the epoch when the emission from the end of the shell reaches the observer (see Fig. 5 for illustration). This gives

$$t_\times \sim \frac{R_\Delta}{\gamma_2^2 c} + \frac{\Delta}{c}. \quad (55)$$

Here  $\Delta = \max(\Delta_0, R/\gamma^2)$ , so our definition is valid throughout the  $(T/t_\gamma)$ – $\sigma$  space. In the  $\sigma \ll 1$  limit, we always have  $R_\Delta / \gamma_2^2 c \sim \Delta/c$ , so that to order-of-magnitude estimate, one can drop the latter term. In the  $\sigma \gg 1$  limit, however, in certain regimes one could have  $R_\Delta / \gamma_2^2 c \ll \Delta/c$ . The correction factor introduced here is therefore essential to delineate the reverse shock behavior in the high- $\sigma$  regime. We note that Nakar & Piran (2004) recently also noticed this correction within the context of the  $\sigma = 0$  regime, although their equation (2) is slightly different from our definition.

In the thick shell regime (I) the reverse shock is relativistic at the crossing radius, and one has  $\gamma_2^2 = \gamma_4 [(n_4/n_1) F]^{1/2}$ . Using the definition of  $R_\Delta$  (eq. [38]), one has  $R_\Delta / \gamma_2^2 c \sim T C_\Delta^2 \sim T Q^{-3/2}$ . Since  $\Delta/c = \Delta_0/c = T$ , with equation (38), we have  $t_\times$  (I)  $\sim t_{\text{dec}}$  (I)  $\sim T(1 + Q^{-3/2})$ . In region II, i.e., the nonspreaing thin shell regime, one has  $\gamma_2 \sim \gamma_4$  and  $\Delta = \Delta_0$ . Using equations (46) and (48), we get  $t_\times$  (II)  $\sim t_\gamma^{3/4} T^{1/4} C_\Delta + T \sim t_\gamma^{3/4} T^{1/4} Q^{-3/4} + T$ . In region III, i.e., the spreading thin shell regime, one has  $\gamma_2 \sim \gamma_4$  and  $\Delta/c = R_\Delta / \gamma_4^2 c$ . With equation (53), one has  $t_\times \sim 2t_\gamma (C_\Delta^2 / C_\gamma) \sim 2t_\gamma Q^{-1}$ .

We define the deceleration time  $t_{\text{dec}}$  as the epoch when the fireball is significantly decelerated. For the thick shell regime (I), this coincides with the shock crossing time. For the thin shell



The strength of this magnetic field component is low, with  $\epsilon_{B,f} \sim 0.01-0.001$ , as inferred from broadband afterglow fits (Panaitescu & Kumar 2002; Yost et al. 2003). For the reverse shock, in the current model the magnetic field is predominantly due to the compression of the upstream magnetic field. Its level depends on the  $\sigma$ -value of the upstream, and the field is globally structured, so the optical flash due to the reverse shock emission (such as the ones observed from GRB 990123 and GRB 021211) should have been strongly polarized (see also Granot & Königl 2003; Fan et al. 2004a; Sagiv et al. 2004).

The forward shock comoving magnetic energy density is defined by

$$\frac{B_f^2}{8\pi} = \frac{B_2^2}{8\pi} = e_2 \epsilon_{B,f}, \quad (60)$$

where  $\epsilon_{B,f}$  is the conventional magnetic equipartition parameter in the afterglow theory, which delineates the fraction of the total internal energy that is distributed to magnetic energy. In the reverse shock region, the comoving magnetic energy density is dominated by the shock-compressed upstream magnetic field and can be denoted as

$$\frac{B_r^2}{8\pi} = \frac{B_3^2}{8\pi} = (f_c - 1) \frac{e_3}{3}, \quad (61)$$

where  $f_c \equiv 1 + p_{b,3}/p_3$  (eq. [30]) has been used. For easy comparison (with respect to the conventional definition of  $\epsilon_{B,f}$ ), we can write equation (61) as

$$\frac{B_r^2}{8\pi} = e_2 \bar{\epsilon}_{B,r}, \quad (62)$$

where

$$\bar{\epsilon}_{B,r} \equiv \frac{f_c - 1}{3f_c} \quad (63)$$

is an artificial parameter to simplify the discussions. With this definition, we can write

$$\mathcal{R}_B \equiv \frac{B_r}{B_f} = \left( \frac{\bar{\epsilon}_{B,r}}{\epsilon_{B,f}} \right)^{1/2}. \quad (64)$$

This is an important parameter that delineates the ratio of the magnetic field strength in the reverse shock and forward shock regions. This ratio has been found to be larger than unity in GRB 990123 and GRB 021211 (e.g., ZKM03), and discussion of this parameter is essential for quantifying the relative emission properties of both shocks.

In Figure 6, we plot  $\bar{\epsilon}_{B,r}$  as a function of  $\sigma$  for both  $\gamma_{34} = 1000$  and  $\gamma_{34} = 1.5$ . We can see that it increases with  $\sigma$  initially, and saturates at a value of  $\frac{1}{3}$  as  $\sigma \gg 1$ . The asymptotic behavior is already obvious in equation (63). We note that the number  $\frac{1}{3}$  is a pure artificial effect given the definition of  $\bar{\epsilon}_{B,r}$  (eq. [62]). The “real” magnetic equipartition factor in region 3 approaches unity when  $\sigma \gg 1$ . In the figure we also plotted the magnetic equipartition parameter in the forward shock region, i.e.,  $\epsilon_{B,f} \sim 0.001$ . This level could also be regarded as the “bottom level” in the  $\sigma \ll 1$  regime for the reverse shock region. The thick lines in Figure 6 are the “total”  $\epsilon_B$  in the reverse shock region (which include both the amplified structured field component and the

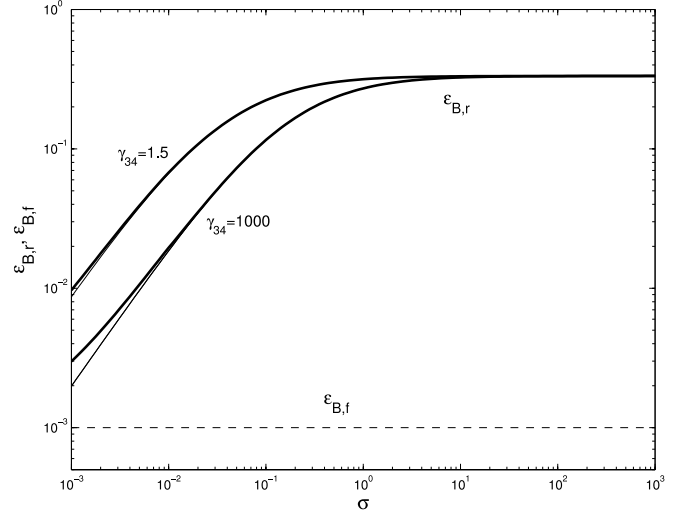


FIG. 6.—Equivalent “magnetic equipartition parameter” in the reverse shock region,  $\bar{\epsilon}_{B,r}$ , as a function of  $\sigma$ , calculated for both  $\gamma_{34} = 1000$  and  $\gamma_{34} = 1.5$ . The dashed line is the assumed magnetic equipartition parameter in the forward shock region, i.e.,  $\epsilon_{B,f} \sim 0.001$ , which is also the “bottom level” for the reverse shock magnetic field in the low- $\sigma$  regime. The thin solid lines are calculated completely from eq. (63), while the thick solid lines include the contribution of the random field in the low- $\sigma$  regime. The fact that the parameter  $\bar{\epsilon}_{B,r}$  approaches  $\frac{1}{3}$  in the high- $\sigma$  regime is only an artificial effect resulting from the definition of  $\bar{\epsilon}_{B,r}$  (eq. [63]).

random field component), which saturates to  $\epsilon_{B,f}$  in the low- $\sigma$  regime.

An interesting conclusion drawn from Figure 6 is that no matter what  $\sigma$  or  $\gamma_{34}$  values are taken, the ratio  $\bar{\epsilon}_{B,r}/\epsilon_{B,f}$  is at most  $\sim 300$  for  $\epsilon_{B,f} \sim 0.001$ . Or effectively, the reverse-to-forward shock magnetic field ratio  $\mathcal{R}_B$  cannot be significantly larger than 15. Since this value was inferred from the case of GRB 990123 (ZKM03), we tentatively conclude that the ejecta in GRB 990123 has  $\sigma > 0.1$  where  $\bar{\epsilon}_{B,r}$  reaches its peak value. The absolute values of  $\epsilon_{B,r}$  and  $\epsilon_{B,f}$  are consistent with those obtained from the detailed modeling. For example,  $\epsilon_{B,f} \sim 7.4 \times 10^{-4}$  was inferred by Panaitescu & Kumar (2002), while  $\epsilon_{B,r}/\epsilon_{B,f} \sim 15^2 \sim 225$  was inferred by ZKM03, so  $\epsilon_{B,r} \sim 0.17$ . This is close to the maximum  $\bar{\epsilon}_{B,r}$  that we have calculated.

#### 4.3. Light-Curve Peak Times and Peak Fluxes

Before describing the detailed process of calculating afterglow light curves, it is informative to define the so-called peak times and peak fluxes. An early optical light curve usually consists of two peaks (ZKM03 and references therein), i.e., a forward shock peak, which corresponds to the epoch when the typical synchrotron frequency crosses the band (Sari et al. 1998; Kobayashi & Zhang 2003a), and a reverse shock peak at which the flux achieves the maximum and starts to decay thereafter. This corresponds to the time when no more shock heating is available and the shell starts to cool adiabatically. The condition for a reverse shock to exist is expressed in equations (31) and (43), and in this paper we focus on the situation when such a condition is satisfied. We denote the reverse (forward) shock peak times and peak fluxes as  $t_{p,r}$  ( $t_{p,f}$ ) and  $F_{\nu,p,r}$  ( $F_{\nu,p,f}$ ), respectively.

For the  $\sigma = 0$  case, the first shock crossing time and the shell deceleration time coincide, so  $t_{p,r} = t_{\times} = t_{\text{dec}}$ . This is still the case when  $\sigma$  is larger, as long as the shell is in the thick shell regime (I). For the thin shell cases (II and III), however, this is no longer the case, and  $t_{\times}$  and  $t_{\text{dec}}$  separate from each other (eqs. [56] and [58]). For easy discussion, hereafter we define the time  $t_{\text{dec}}$  as

the reverse shock peak time and its corresponding afterglow flux as the reverse shock peak flux, i.e.,

$$\begin{aligned} t_{p,r} &= t_{\text{dec}}, \\ F_{\nu,p,r} &= F_{\nu}(t_{\text{dec}}). \end{aligned} \quad (65)$$

For  $t > t_{p,r}$ , the shell cools adiabatically, and a decaying light curve results.<sup>10</sup> The  $t < t_{p,r}$  case is a little more complicated. For the thick shell case (I), since  $t_{\times}$  coincides with  $t_{p,r}$ , it is a rising light curve due to shock crossing. For the thin shell cases (II and III), as demonstrated above, the shell is heated at first shock crossing and remains heated until it is significantly decelerated. This results in a broad reverse shock peak that starts at  $t_{\times}$  and ends at  $t_{p,r}$ . Much more detailed studies are needed to reveal the physics during this stage, but to a first-order estimate, in this paper we assume that the heating level between  $t_{\times}$  and  $t_{p,r}$  is roughly the same, so that the light curve shows a plateau during this period.

To calculate the synchrotron radiation flux, one needs to quantify the comoving random Lorentz factor of the leptons. We still take the convention of assuming that the shock-accelerated leptons have a single power-law distribution with the indices  $p_f$  and  $p_r$  for the forward and the reverse shocks, respectively, and that they occupy a fraction  $\epsilon_{e,f}$  and  $\epsilon_{e,r}$  of the total thermal energy in the forward shock region (which is  $e_2$ ) and in the reverse shock region (which is  $e_3$ ), respectively. For the reverse shock region, the lepton density may be enriched by the presence of pairs generated in the prompt emission phase (e.g., Li et al. 2003b). The pair multiplicity parameter

$$y \equiv \frac{N_b + N_{\pm}}{N_b} \geq 1 \quad (66)$$

may be of order unity or mildly large in the low- $\sigma$  regime (depending on the compactness of the region when the prompt gamma rays are emitted; e.g., Kobayashi et al. 2002; Mészáros et al. 2002) and could be very large in the high- $\sigma$  regime (e.g., Zhang & Mészáros 2002). In this paper, we are mainly focusing on the novel features introduced by the  $\sigma$ -parameter, and we take  $y \sim 1$  in the following calculations. The  $y$ -dependences are included in the expressions, and their implication are discussed in § 4.4.

The minimum comoving electron energy in the region “ $i$ ” (2 or 3) is  $\gamma_{e,m,i} = (\epsilon_{e,i}/y_i)(e_i/n_i m_p c^2)g(p_i)(m_p/m_e)$ , where  $g(p) = (p-2)/(p-1)$  (assuming  $p > 2$ ). Taking the values at the first shock crossing time  $t_{\times}$ , one gets

$$\frac{\gamma_{e,m,r}(t_{\times})}{\gamma_{e,m,f}(t_{\times})} = \left( \frac{\epsilon_{e,r} g_r}{y \epsilon_{e,f} g_f} \right) f_a \frac{\gamma_{34}(t_{\times}) - 1}{\gamma_2(t_{\times}) - 1} \sim \mathcal{R}_e f_a \frac{\gamma_0}{\gamma_{\times}^2} y^{-1}, \quad (67)$$

where we have defined

$$\mathcal{R}_e \equiv \frac{\epsilon_{e,r} g_r}{\epsilon_{e,f} g_f}, \quad (68)$$

used  $\gamma_{34} \sim \gamma_4/\gamma_2(\times)$  (which is valid for both thick and thin shells), and replaced  $\gamma_4$  and  $\gamma_2(\times)$  by  $\gamma_0$  (which means the initial Lorentz factor) and  $\gamma_{\times}$  (the fireball Lorentz factor at the shock

crossing time), respectively.<sup>11</sup> This allows the same notation system as in our previous work (ZKM03).

We are more interested in the behavior at the reverse shock peak time (i.e., the deceleration time),  $t_{p,r}$ . For the thick shell case, this is simply  $t_{\times}$ . For the thin shell case, after the first shock crossing, the shell is kept heated by the multicrossing of successive shocks. To first order, we can take the approximation that the heating level in the ejecta during the time period between  $t_{\times}$  and  $t_{p,r}$  is approximately constant; i.e.,  $e_3/n_3 \propto t^0$ . During the same period the random Lorentz factor in the shocked ISM region also remains constant (since  $\gamma_2 \sim \gamma_4$  before deceleration); we therefore also have

$$\frac{\gamma_{e,m,r}(t_{p,r})}{\gamma_{e,m,f}(t_{p,r})} \sim \frac{\gamma_{e,m,r}(t_{\times})}{\gamma_{e,m,f}(t_{\times})} \sim \mathcal{R}_e f_a \frac{\gamma_0}{\gamma_{\times}^2} y^{-1}, \quad (69)$$

which is valid for both the thick and thin shell cases.

Let us denote the total electron numbers in the forward and reverse shocked region as  $N_{e,f}$  and  $N_{e,r}$ , respectively. In the reverse shock region, the total lepton number (now including pairs) is  $N_{e,r} = N_b + N_{\pm} = yN_b$ , where the definition in equation (66) is used. According to equation (40), at the deceleration radius, the total energy in the forward shock region is defined by  $E_K$  alone. Although the bulk of the Poynting energy is expected to be transferred to the ISM eventually, shortly after the shock crossing and near the forward shock peak, this correction may not be significant. Below we ignore this process in our calculations of the forward shock emission, but keeping in mind that the real forward shock emission level would increase with time and may be much higher than our predicted level at later times. When we focus on early afterglow light curves, our calculations should be close to the real emission level (see more discussions in Zhang & Kobayashi 2005). A more careful treatment will be presented in a future work.

In our approximated treatment, one can write  $E_K = \gamma_0 c^2 (N_b m_p + N_{\pm} m_e) \sim \gamma_0 N_b m_p c^2 \sim N_{e,f} m_p c^2 [\gamma(t_{\text{dec}})]^2 \sim N_{e,f} m_p c^2 \gamma_{\times}^2$ , where we have assumed  $y \ll m_p/m_e$ , so that the total pair mass  $N_{\pm} m_e$  is much smaller than the total baryon mass  $N_b m_p$ . This gives

$$\frac{N_{e,r}(t_{p,r})}{N_{e,f}(t_{p,r})} \sim y \frac{\gamma_{\times}^2}{\gamma_0}. \quad (70)$$

The characteristic synchrotron emission frequency is  $\nu_m \propto \gamma B \gamma_{e,m}^2$ , the cooling frequency is  $\nu_c \propto \gamma^{-1} B^{-3} t^{-2}$ , and the peak specific flux is  $F_{\nu,m} \propto \gamma B N_e$ , where  $\gamma$  is the bulk Lorentz factor. For the thin shell case, we also make another approximation that  $B_3$  stays constant from  $t_{\times}$  to  $t_{\text{dec}}$  [so that  $\mathcal{R}_B(t_{\times}) \simeq \mathcal{R}_B(t_{\text{dec}}) = \mathcal{R}_B$ ]. Similar to Kobayashi & Zhang (2003a) and ZKM03, we can finally derive the following relations at  $t_{\text{dec}}$ :

$$\frac{\nu_{m,r}(t_{p,r})}{\nu_{m,f}(t_{p,r})} \sim \hat{\gamma}^{-2} \mathcal{R}_e^2 \mathcal{R}_B f_a^2 y^{-2}, \quad (71)$$

$$\frac{\nu_{c,r}(t_{p,r})}{\nu_{c,f}(t_{p,r})} \sim \mathcal{R}_B^{-3}, \quad (72)$$

$$\frac{F_{\nu,m,r}(t_{p,r})}{F_{\nu,m,f}(t_{p,r})} \sim \hat{\gamma} \mathcal{R}_B y, \quad (73)$$

<sup>11</sup> Strictly speaking, the last factor  $\gamma_0/\gamma_{\times}^2$  in equation (67) should be  $(\gamma_0 - \gamma_{\times})/\gamma_{\times}^2$ . The current approximation is valid as long as the reverse shock is mildly relativistic, say,  $\gamma_{34} > 1.5$ . For an even smaller  $\gamma_{34}$  (which could be possible when  $\sigma$  is large enough), there should be an additional correction factor (less than unity) in both eqs. (67) and (69).

<sup>10</sup> When  $\sigma$  is very large, additional heating for the shell may still happen if the post-shock crossing energy transfer process timescale is short enough.

where

$$\hat{\gamma} \equiv \frac{\gamma_x^2}{\gamma_0} = \min\left(\gamma_0, \frac{\gamma_c^2}{\gamma_0}\right) \leq \gamma_c. \quad (74)$$

Although there are, in principle, many cases of the reverse shock emission light curves (Kobayashi 2000), within the reasonable parameter regime the light-curve behavior only has two variations, depending on whether  $\mathcal{R}_\nu > 1$  or  $\mathcal{R}_\nu < 1$  (ZKM03), where

$$\mathcal{R}_\nu \equiv \frac{\nu_R}{\nu_{m,r}(t_{p,r})}. \quad (75)$$

In both cases, the ratio between the two peak-time fluxes

$$\mathcal{R}_F \equiv \frac{F_{\nu,p,r}}{F_{\nu,p,f}} \quad (76)$$

and the ratio between the two peak times

$$\mathcal{R}_t \equiv \frac{t_{p,f}}{t_{p,r}} \quad (77)$$

can be expressed in terms of  $\hat{\gamma}$ ,  $\mathcal{R}_B$ , and  $\mathcal{R}_\nu$ , respectively, for the  $\sigma = 0$  case (ZKM03). Here the forward shock peak time  $t_{p,f}$  corresponds to the epoch when  $\nu_{m,f}$  crosses the band.

Below we repeat this process but focus more on corrections introduced by the  $\sigma$ -factor. To further simplify the problem, we first estimate the numerical value of  $\mathcal{R}_\nu$ . Due to the complication introduced by the  $\sigma$ -parameter, one cannot coast  $\mathcal{R}_\nu$  into a simple expression as in the  $\sigma = 0$  case (e.g., eq. [24] in ZKM03). In any case, using equation (71) and the standard expression for  $\nu_{m,f}(t)$  (e.g., eq. [1] in Kobayashi & Zhang 2003a), one can write

$$\begin{aligned} \mathcal{R}_\nu &\sim 800 \mathcal{R}_B^{-1} f_a^{-2} y^2 \mathcal{R}_e^{-2} \left(\frac{kE_K}{10^{52} \text{ ergs}}\right)^{-1/2} \left(\frac{\hat{\gamma}_2}{100}\right)^2 \\ &\times \left(\frac{\epsilon_{B,f}}{0.001}\right)^{-1/2} \left(\frac{\epsilon_{e,f}}{0.1}\right)^{-2} \left(\frac{g_f}{1/3}\right)^{-2} \\ &\times \left(\frac{t_{\text{dec}}}{100 \text{ s}}\right)^{3/2} \left(\frac{1+z}{2}\right)^{-1/2}. \end{aligned} \quad (78)$$

For  $\hat{\gamma} \leq \gamma_c \sim 125$  (eq. [52]),  $\mathcal{R}_e \sim 1$ ,  $y \geq 1$ , and  $f_a < 1$ , the above equation therefore essentially always gives  $\mathcal{R}_\nu > 1$ . In the following discussions, we do not discuss the  $\mathcal{R}_\nu < 1$  case any further (which was also discussed in ZKM03).

The reverse shock emission light curve in the  $\mathcal{R}_\nu > 1$  case is simple. The light curve initially rises and reaches the peak at  $t_x$ . The flux level then stays essentially constant until  $t_{p,r}$  (for the thick shell case, both timescales coincide, so there is no broadened peak) and starts to decay after  $t_{p,r}$ . The temporal indices of each segment of the light curve are also well defined. In the rising part of the light curves, since all the correction factors introduced by the  $\sigma$ -parameter are essentially time independent, the corrections essentially do not introduce extra time dependence on the typical frequencies and the peak flux of the synchrotron radiation in the reverse shock. The rising light curves essentially remain unchanged as in the  $\sigma = 0$  case, as has been derived by Kobayashi (2000). This gives a  $\sim \frac{1}{2}$  temporal index for the thick shell case and a  $\sim 5$  temporal index for the thin shell case.<sup>12</sup> After

the deceleration time, the shell cools. The optical band is typically in the regime of  $\nu_{m,r}(t_x) < \nu_R < \nu_{c,r}(t_x)$ . After the deceleration time, one has  $\nu_{m,r} \propto t^{-3/2}$ ,  $F_{\nu,m,r} \propto t^{-1}$  (Kobayashi 2000).<sup>13</sup> Thus, the temporal decay index (i.e.,  $F_\nu \propto t^{-\alpha}$ ) is

$$\alpha = \frac{3p_r + 1}{4} \sim 2, \quad (79)$$

where  $p_r$  is the electron power-law index in the reverse shock region.

For  $t > t_{p,r}$ , one has  $\nu_{m,f} \propto t^{-3/2}$ ,  $F_{\nu,m,f} \propto t^0$  (Mészáros & Rees 1997a)<sup>14</sup> and  $\nu_{m,r} \propto t^{-3/2}$ ,  $F_{\nu,m,r} \propto t^{-1}$  (Kobayashi 2000). Using the definitions of  $\mathcal{R}_\nu$ ,  $\mathcal{R}_F$ , and  $\mathcal{R}_t$  (eqs. [75]–[77]), as well as equations (71) and (73), one can derive<sup>15</sup>

$$\mathcal{R}_t = \hat{\gamma}^{4/3} \mathcal{R}_B^{-2/3} \mathcal{R}_\nu^{-2/3} (\mathcal{R}_e^{-4/3} y^{4/3} f_a^{-4/3}), \quad (80)$$

$$\mathcal{R}_F = \hat{\gamma} \mathcal{R}_B \mathcal{R}_\nu^{-2(\alpha-1)/3} (y). \quad (81)$$

These are valid for all three parameter regions in Figure 4. Comparing with equations (12) and (13) in ZKM03, the extra correction factors are presented in parentheses. Note that the correction factors  $\mathcal{R}_e$  and  $y$  should also exist in the  $\sigma = 0$  case, but we have previously assumed them to be unity. The extra  $\sigma$ -dependent correction factors are  $f_a^{-4/3}$  and  $\mathcal{R}_\nu$  (which is modified by the  $\sigma$ -parameter through many factors, e.g.,  $\mathcal{R}_B$ ,  $f_a$ ,  $E_K$ , and  $t_{\text{dec}}$ ; see eq. [78]).

#### 4.4. Sample Light Curves

We now calculate the typical early optical afterglow light curves for various parameter regimes. Equation (40) states that the initial afterglow energy, which is essentially the kinetic part of the total energy, decreases with  $\sigma$  given a constant total energy  $E = E_K + E_p$ . At high  $\sigma$ , not only does the reverse shock flux level drop, but the forward shock flux level shortly after the shock crossing also decreases steadily. At later times, the forward shock level would increase due to magnetic energy injection. Since we are focusing on the early afterglow emission, this effect is neglected in the following discussions. To explore the  $\sigma$ -effect, we fix the total energy of the fireball so that  $E_K$  decreases with increasing  $\sigma$ . To simplify the calculations, we assume  $\mathcal{R}_e \sim 1$  and  $y \sim 1$ . The input parameters we adopt include  $E_{52} = 1$ ,  $\gamma_0 = 150$ ,  $n = 1$ ,  $\epsilon_{e,f} = 0.1$ ,  $\epsilon_{B,f} = 0.001$ ,  $p_f = 2.2$ , and  $z = 1$  (with the standard cosmological parameters  $\Omega_\Lambda \sim 0.7$ ,  $\Omega_m \sim 0.3$ , and  $H_0 \sim 70 \text{ km s}^{-1} \text{ Mpc}^{-1}$ ). This gives the forward shock peak time and flux (Sari et al. 1998; Kobayashi & Zhang 2003a)

$$t_{p,f} \sim 1000 \text{ s}, \quad (82)$$

$$F_{p,f} \sim 1.7(1 + \sigma)^{-1} \text{ mJy} \quad [m_R \sim 15.6 + 2.5 \log(1 + \sigma)]. \quad (83)$$

<sup>13</sup> A more detailed discussion such as that presented in Kobayashi & Sari (2000) leads to a similar conclusion.

<sup>14</sup> Note again that here we have assumed that the energy transfer timescale from a Poynting flux to the kinetic energy of the ISM long enough. This forward shock emission level should be regarded as a lower limit when the energy transfer process is taken into account.

<sup>15</sup> In ZKM03, we have defined  $\mathcal{R}_F$  and  $\mathcal{R}_t$  at  $t_x$ , but in the  $\sigma = 0$  case one has  $t_x = t_{\text{dec}}$ . For the case of an arbitrary  $\sigma$ , the deceleration time  $t_{\text{dec}}$  is more fundamental to defining the problem.

<sup>12</sup> Detailed numerical calculations result in non-power-law behavior in the rising light curve (Fan et al. 2004a).

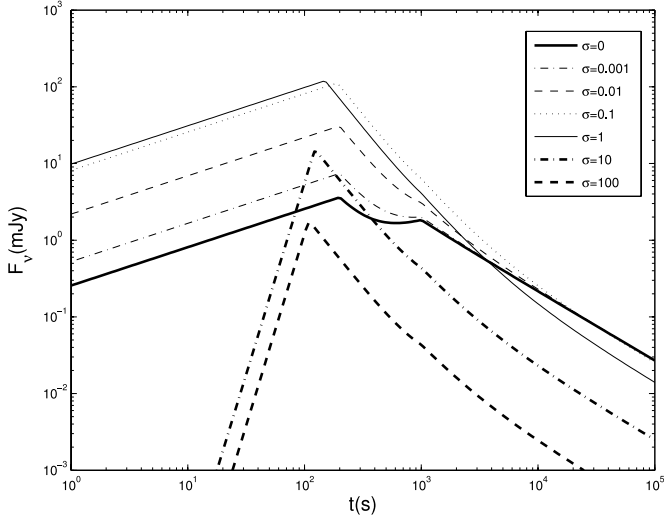


FIG. 7a

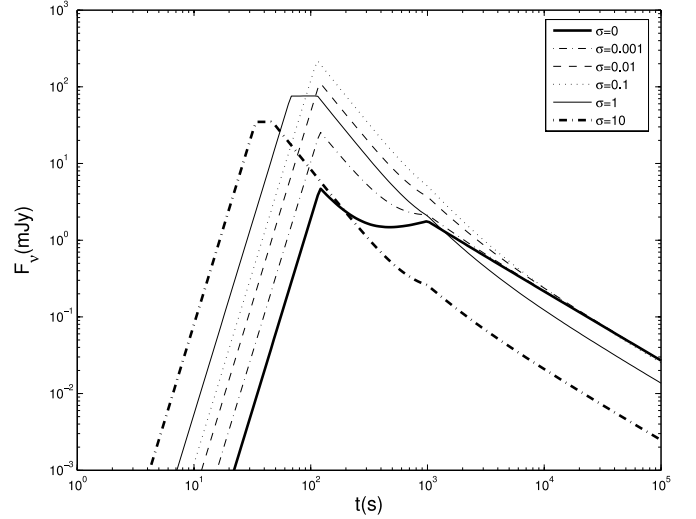


FIG. 7b

FIG. 7.—Sample early afterglow light curves for GRBs with an arbitrary magnetization parameter  $\sigma$ . The following parameters are adopted:  $E_{52} = 1$ ,  $\gamma_0 = 150$ ,  $n = 1$ ,  $\epsilon_{e,f} = 0.1$ ,  $\epsilon_{B,f} = 0.001$ ,  $p_f = 2.2$ , and  $z = 1$ . We also take  $\mathcal{R}_e \sim 1$  and  $y \sim 1$ . Both the forward shock and the reverse shock emission components are calculated, and they are superposed to get the final light curve. For the forward shock emission component we assumed that the timescale for the energy transfer from the Poynting energy to the afterglow energy is long enough that the forward shock level is defined by  $E_K$  only, and its level decreases with  $\sigma$ . This approximation is good shortly after the reverse shock crossing. At later times, the real level could be progressively higher than this level and the calculation should be regarded as a lower limit. Light curves are calculated for different  $\sigma$ -values. *Thick solid line*:  $\sigma = 0$ ; *thin dash-dotted line*:  $\sigma = 0.001$ ; *thin dashed line*:  $\sigma = 0.01$ ; *thin solid line*:  $\sigma = 0.1$ ; *thick dash-dotted line*:  $\sigma = 10$ ; *thick dashed line*:  $\sigma = 100$ . The value  $\gamma_{34} = 1.5$  has been assumed for thin shell regimes. For high- $\sigma$  cases,  $\gamma_{34}$  is closer to unity, and the reverse shock peak flux should be further suppressed. (a)  $T = 100$  s case. According to equation (43), the reverse shock exists when  $\sigma < 200$ . (b)  $T = 20$  s case. The condition for the existence of the reverse shock is  $\sigma < 20$ .

We also have  $t_\gamma = [(3E/4\pi\gamma_0^2 n m_p c^2)^{1/3}/2\gamma_0^2 c](1+z) \sim 60$  s. (For this calculation, we have added in all the precise coefficients previously neglected.) We then take two typical values of GRB durations. For the first case, we take  $T = 100$  s. When  $\sigma$  is small the burst is in the thick shell regime (region I). As  $\sigma$  increases, the burst is in the nonspreading thin shell regime (region II). For the second case, we take  $T = 20$  s. The burst is always in the thin shell regime for any  $\sigma$ -value, but transforms from the spreading thin shell regime (region III) to the nonspreading thin shell regime (region II) when  $\sigma$  is large enough.

For each  $T$  value, we calculate both the reverse shock and the forward shock light curve for several values of  $\sigma$ , i.e.,  $\sigma = 0, 0.001, 0.01, 0.1, 1, 10$ , and  $100$  (Fig. 7), as long as the condition for the existence of the reverse shock (eq. [43]) is satisfied. The procedure of our calculation is the following. First, with  $t_\gamma$ ,  $T$ , and the assumed  $\sigma$ , one can judge which parameter region the burst is in. With this information one can then calculate  $t_{\text{dec}} = t_{p,r}$  and  $\mathcal{R}_t$  for both the thick and thin shell regimes, as well as  $t_\times$  for the thin shell case. Next, we calculate  $\mathcal{R}_B$  with the assumed  $\sigma$ -value (Fig. 6). For the thick shell case, we use the  $\bar{\epsilon}_B$  value for  $\gamma_{34} \sim 1000$ , since  $\bar{\epsilon}_B$  is insensitive to  $\gamma_{34}$  when it is large. For the thin shell case we use the  $\bar{\epsilon}_B$  value for  $\gamma_{34} \sim 1.5$ , exclusively.<sup>16</sup> One can then solve  $\mathcal{R}_\nu$  (eq. [80]) and then use the value of  $\mathcal{R}_\nu$  to calculate  $\mathcal{R}_F$  (eq. [81]), and hence  $F_{\nu,p,r}$ . Since we know the temporal indices of the reverse shock light curve during the rising ( $\sim \frac{1}{2}$  for thick shell and  $\sim 5$  for thin shell; Kobayashi 2000) and the decaying phases ( $\sim -1.9$  for  $p_r = 2.2$ ), the reverse shock light curve can be calculated once  $t_{p,r} = t_{\text{dec}}$  and  $F_{\nu,p,r}$  are known. For the thin shell case, with the current approximation, we roughly keep  $F_\nu$  a constant between  $t_{\times,t}$  and  $t_{\text{dec}}$ , both of which are known. For the forward shock emission, the temporal index is  $3(1 - p_f)/4$  ( $\sim 0.9$  for  $p_f = 2.2$ ) after the peak time and

<sup>16</sup> Note that in reality, when  $\sigma$  is very large,  $\gamma_{34}$  could be much closer to unity. In such cases, the reverse shock peak flux should be further suppressed.

is  $\frac{1}{2}$  before the peak time (but after the deceleration time).<sup>17</sup> Given  $F_{p,f}$  (which is dependent on  $\sigma$ ; eq. [83]), the forward shock light curve is also calculated.

Some sample  $R$ -band early afterglow light curves are presented in Figure 7, with the contributions from both the reverse and the forward shocks superposed. For the forward shock emission component we assume that the timescale for the energy transfer from the Poynting energy to the afterglow energy is long enough, so that the forward shock level is defined by  $E_K$  only, and its level decreases with  $\sigma$ . This approximation is good shortly after the reverse shock crossing. At later times, the real level could be progressively higher than this level and the calculation should be regarded as a lower limit (see Zhang & Kobayashi 2005 for more explanations). In Figure 7a, the cases for  $T = 100$  s are calculated. According to equation (43), a reverse shock exists as long as  $\sigma < 200$ . We therefore calculate the light curves up to  $\sigma = 100$ . We can see that for  $\sigma \leq 1$ , the parameters are in the thick shell (relativistic reverse shock) regime. When  $\sigma$  increases from below, the contrast between the reverse and forward shock peak fluxes (i.e.,  $\mathcal{R}_F$ ) increases steadily. Since the forward shock emission level does not change much when  $\sigma < 1$ , the reverse shock peak flux increases steadily with  $\sigma$ . At even higher  $\sigma$ -values, the reverse shock peak flux drops steadily with  $\sigma$ . In the meantime, the burst enters the thin shell regime so that the separation between  $t_\times$  and  $t_{\text{dec}}$  becomes wider, and the reverse shock emission has a broader peak. In Figure 7b, the cases for  $T = 20$  s are calculated. According to equation (43), a reverse shock exists as long as  $\sigma < 20$ , and we calculate the light

<sup>17</sup> Before the deceleration time, the forward shock light curve should have different temporal slopes. During the shock crossing, we have  $\gamma_2 \propto t^0$  for thin shells and  $\gamma_2 \propto t^{-1/4}$  for thick shells. Using the standard synchrotron radiation analysis (e.g., Sari et al. 1998), the forward shock emission temporal slope is 3 and 4/3 for the thin and thick shell cases, respectively. Between the shock crossing time and the deceleration time in the high- $\sigma$  thin shell case, the temporal slope is flat.

curves up to  $\sigma = 10$ . The shell is in the thin shell regime throughout the whole  $\sigma$ -range calculated. The transition from spreading to nonspreading thin shell regime does not bring any noticeable signature in the light curves. Again, the reverse shock peak flux increases with  $\sigma$  initially (when  $\sigma \leq 0.1$ ) and starts to decrease when  $\sigma \geq 0.1$ . The reverse shock peak is broad, but the separation gradually shrinks due to the decrease of the  $(Q^{-1/2} - Q^{-1})$  parameter (eq. [59]). Throughout our calculations,  $\mathcal{R}_\nu$  remains larger than 25 (up to  $\sim 1000$  for  $\sigma = 0$  in the  $T = 100$  s case), so our treatment by neglecting the  $\mathcal{R}_\nu < 1$  regime is justified.

We notice several interesting features from our results. First, the reverse shock component is still noticeable even with  $\sigma \gtrsim 1$  (until it reaches several tens or even hundreds when condition (43) is no longer satisfied). The absolute reverse shock peak flux increases with  $\sigma$  initially but drops steadily when  $\sigma > 1$ . Second, the forward shock emission level right after shock crossing also drops with  $\sigma$ . This is because only the kinetic energy of the baryonic component ( $E_K$ ) defines the afterglow level after the shock crossing time. The forward shock level will increase later due to the transfer of the remaining magnetic energy into the medium. One then expects an initially dim early afterglow for a high- $\sigma$  flow, which would be brightened at later times. If GRB prompt emission is due to magnetic dissipation (e.g., Drenkhahn & Spruit 2002) and if  $\sigma$  is still high in the afterglow phase (e.g.,  $\sim 10$ ), one might be able to account for the very large apparent GRB efficiencies inferred from some GRBs (e.g., Lloyd-Ronning & Zhang 2004). Such a picture may also be relevant to the recent December 27 giant flare afterglow from the soft gamma-ray repeater 1806-20, for which a very high gamma-ray efficiency is inferred (Wang et al. 2005 and references therein). Third, the broad reverse shock peak is a novel feature identified in the high- $\sigma$  model; it can be used to diagnose the existence of a Poynting flux-dominated flow. The physical origin of the broad peak is that a high  $\sigma$ -value leads to the decoupling of the shock crossing radius  $R_x$  and the deceleration radius  $R_\gamma$ , so that multicrossing of a series of successive shocks leads to continuous heating of the ejecta shell before cooling starts.

In the above calculations,  $y = 1$  has been adopted (i.e., we assume that the pair fraction is negligible in the ejecta). In some cases, especially in the high- $\sigma$  regime,  $y$  could be much larger than unity. It would be essential to investigate the  $y$ -dependence of the current analysis. We solve  $\mathcal{R}_\nu$  from equation (80) and submit it to  $\mathcal{R}_F$ , and we find  $\mathcal{R}_F \propto y^{(7-4\alpha)/3}$ , which is  $\propto y^{-1/3}$  for  $\alpha = 2$ . We can see that a larger  $y$  will lower the reverse-to-forward shock peak flux contrast, although the dependence is mild. The  $\mathcal{R}_F$  factor is more sensitive to  $\mathcal{R}_e$  (i.e.,  $\propto \mathcal{R}_e^{4(\alpha-1)/3}$ ), but assuming a similar shock acceleration mechanism,  $\mathcal{R}_e$  may not deviate too much from unity.

Our results can be directly compared with the early afterglow data of the four bursts for which such information is available so far. The case of GRB 990123 (Akerlof et al. 1999) is consistent with a flow with  $0.1 < \sigma < 1$  in which regime  $\mathcal{R}_F$  is large and the reverse shock peak is not broadened. The observed bright afterglow also argues against a higher  $\sigma$  flow. The case of GRB 021211 (Fox et al. 2003b; Li et al. 2003a) also shows a large  $\mathcal{R}_F$ , which also suggests that  $\sigma > 0.1$ . For GRB 021004, Kobayashi & Zhang (2003a) attempted to fit the data with the  $\sigma = 0$ ,  $\mathcal{R}_B = 1$  model. Another data point at an earlier epoch after the burst trigger reported by Fox et al. (2003a) makes that model more difficult to fit, and it has been attributed to a continuous energy injection (Fox et al. 2003a) or to the emission from a wind-type medium (Li & Chevalier 2003). However, using the theory developed in this paper, the data may be consistent with a high- $\sigma$  flow (e.g.,  $\sigma \gtrsim 10$ ), so the extended early afterglow emission

could be interpreted as the combination of the broad reverse shock peak and the gradual transfer of the Poynting energy into the afterglow energy. In the high- $\sigma$  regime, the  $(\gamma_{34} - 1)$  is quite small during the shock crossing, which will lower the reverse shock peak flux and  $\mathcal{R}_F$ . Similarly, a broad early afterglow bump was identified in GRB 030418 (Rykoﬀ et al. 2004), which challenges the conventional reverse shock model but may be consistent with a high- $\sigma$  flow (weak or no reverse shock component). Although detailed modeling is needed (we plan to do it in a future work), we tentatively conclude that all the current early optical afterglow data may be understood within the theoretical framework developed in this paper, if  $\sigma$  is allowed to vary for different GRB fireballs.

## 5. CONCLUSIONS AND DISCUSSION

We have derived a rigorous analytical solution for the relativistic  $90^\circ$  shocks under the ideal MHD condition (eq. [A16]). Generally, the solution depends both on the magnetization  $\sigma$ -parameter and the Lorentz factor of the shock,  $\gamma_{12}$ . The solution can be reduced to the Blandford-McKee hydrodynamical solution when  $\sigma = 0$  and to the Kennel-Coroniti solution (which depends on  $\sigma$  only) when the  $\gamma_{21} \gg 1$ . Our generalized solution can be used to treat the more general cases, e.g., when the reverse shocks upstream and downstream are mildly relativistic with each other. Since GRBs invoke a shell with finite width, this latter possibility is common (e.g., the parameter space for thin shell greatly increases in the high- $\sigma$  regime), so our generalized solution is essential to deal with the GRB reverse shock problem.

Several interesting conclusions emerge from our analysis. (1) Strong shocks still exist in the high- $\sigma$  regime, as long as the shock is relativistic. Figures 2c and 2d indicate that as  $\sigma$  increases, both the downstream ‘‘temperature’’  $e_2/n_2$  and the ‘‘shock compression factor’’  $n_2/n_1$  decrease with respect to the  $\sigma = 0$  values. However, the suppression factors in both cases are only mild (a factor of  $\sim 0.5$ ), and they saturate when  $\sigma \gg 1$ . In the relativistic shock regime, the results are actually consistent with Kennel & Coroniti (1984). However, these authors did not calculate the suppression factor with respect to the  $\sigma = 0$  case and did not explore further into the high- $\sigma$  regime, so their results leave readers the impression that the shock is completely suppressed when  $\sigma$  reaches higher values. For typical GRB parameters, we found that a reverse shock still exists when  $\sigma$  is as high as several tens or even hundreds. When the reverse shock exists, its emission level decreases when  $\sigma$  gets higher. This is not only because the reverse shock becomes weaker since  $\gamma_{34}$  gets close to unity in the high- $\sigma$  regime but also because the total kinetic energy in the flow (which is the energy reservoir for shock dissipation) gets smaller given the same total energy. (2) During ejecta-medium interaction, somewhat surprisingly, some important parameters, such as  $F$  and  $C_\Delta$ , are very insensitive to the reverse shock Lorentz factor,  $\gamma_{34}$ , and can be regarded as a function of  $\sigma$  only (§§ 2.3 and 3.3). This greatly simplifies the problem and is essential for characterizing the parameter regimes. (3) The triple coincidence of the first three critical lines in equation (49) is very crucial for a self-consistent description of the problem (§ 3.3).

Comparing with the conventional hydrodynamical treatment, we reveal several novel features for the early light curves. First, as  $\sigma$  increases, the reverse shock peak flux initially increases rapidly, reaching a peak around  $\sigma \sim 0.1-1$ , and starts to decrease when  $\sigma \geq 1$ . Second, due to the inability to tap the Poynting flux energy during the shock crossing process, the fireball deceleration radius decreases as  $\sigma$  increases [ $\propto (1 + \sigma)^{-1/3}$ ]. The forward shock emission level is also lower right after shock crossing. Third, in the high- $\sigma$  thin shell regime, the reverse shock peak is

broadened due to the separation of the shock crossing radius and the deceleration radius. This is a signature for a high- $\sigma$  flow, which can be used to diagnose the magnetic content of the fireball. Fourth, as  $\sigma$  becomes large enough (larger than several tens or several hundreds), the condition for forming a reverse shock is no longer satisfied, and there should be no reverse shock component in the early afterglow light curves. This could be consistent with very early tight optical upper limits for some GRBs, such as the recent *Swift* dark burst GRB 050319a (P. Roming et al. 2005, in preparation). In summary, the above new features allow the current theory to potentially interpret known GRB early afterglow cases collected so far, as well as the case of the dark bursts, if one allows  $\sigma$  to vary in a wide enough range (say, from 0.01 to 100). The *Swift* GRB mission, launched on 2004 November 20, is expected to detect many early optical afterglow light curves with the UV-optical telescope on board. We expect to further test our theoretical predictions against the abundant *Swift* data and to systematically diagnose the magnetic content of GRB fireballs.

If the GRB ejecta is indeed magnetized, as inferred from the early afterglow data, the internal shocks should also be corrected by the magnetic suppression factor. This aspect has been investigated recently by Fan et al. (2004b).

Throughout the paper, we have treated the problem under the ideal MHD limit. In the high- $\sigma$  case, strong magnetic dissipation may occur. The magnetic dissipation effect has been included in the internal shock study of Fan et al. (2004b). Our treatment in this paper presents a first-order picture to the early afterglow problem (see also Fan et al. 2004a, whose treatment in the mildly magnetized regime is consistent with ours), and further considerations are needed to fully delineate the physics involved. In

addition, our whole discussion is relevant when a reverse shock is present. It does not apply to the regime for an even higher  $\sigma$ -value (e.g., Lyutikov & Blandford 2003). Finally, as discussed in § 4.1, further studies on particle acceleration in MHD shocks are essential to give a more accurate calculation of the reverse shock emission in the high- $\sigma$  regime.

We only discussed one type of the medium, i.e., one with an assumed constant medium density, typically for the interstellar medium. In principle, the medium density can vary with distance from the central engine. In particular, a wind-type medium, characterized by the  $n \propto R^{-2}$  profile, has been widely discussed. Our MHD shock theory could be straightforwardly used for the wind case to study the reverse shock emission in combination with the previous pure hydrodynamical treatments (Chevalier & Li 2000; Wu et al. 2003; Kobayashi & Zhang 2003b; Kobayashi et al. 2004; see Fan et al. 2004a for a preliminary treatment).

We thank the anonymous referee for a thorough check of the scientific content of the paper, Y. Z. Fan and M. Lyutikov for important remarks and in-depth discussions, P. Mészáros, L. J. Gou, and D. M. Wei for helpful comments, and C. Akerloff, M. G. Baring, R. D. Blandford, D. Fox, C. Kouveliotou, P. Kumar, J. Granot, E. Nakar, T. Piran, R. Sari, A. Spitkovsky, M. J. Rees, E. Rykoff, and W. Zhang for discussions. This work is supported by NASA grants NNG04GD51G and NAG5-13286 (for B. Z.), by Penn State Center for Gravitational Wave Physics through NSF PHY 01-14375, and by Eberly Research Fund of Penn State University (for S. K.) and by a *Swift* GI (Cycle 1) theory program (for both authors).

## APPENDIX A

### DERIVATION OF THE SOLUTION OF THE RELATIVISTIC 90° SHOCK JUMP CONDITIONS

#### A1. LORENTZ TRANSFORMATIONS

Given the definitions of  $\gamma_{ij}$ ,  $\beta_{ij}$ , and  $u_{ij}$ , the following Lorentz transformations are frequently used in the derivations.

$$\beta_{2s} = \frac{\beta_{1s} - \beta_{21}}{1 - \beta_{1s}\beta_{21}}, \quad (\text{A1})$$

$$\beta_{1s} = \frac{\beta_{2s} + \beta_{21}}{1 + \beta_{2s}\beta_{21}}, \quad (\text{A2})$$

$$\beta_{21} = \frac{\beta_{1s} - \beta_{2s}}{1 - \beta_{1s}\beta_{2s}}, \quad (\text{A3})$$

$$\gamma_{2s} = \gamma_{1s}\gamma_{21}(1 - \beta_{1s}\beta_{21}), \quad (\text{A4})$$

$$\gamma_{1s} = \gamma_{2s}\gamma_{21}(1 + \beta_{2s}\beta_{21}), \quad (\text{A5})$$

$$\gamma_{21} = \gamma_{1s}\gamma_{2s}(1 - \beta_{1s}\beta_{2s}), \quad (\text{A6})$$

$$u_{2s} = \gamma_{1s}\gamma_{21}(\beta_{1s} - \beta_{21}), \quad (\text{A7})$$

$$u_{1s} = \gamma_{2s}\gamma_{21}(\beta_{2s} + \beta_{21}), \quad (\text{A8})$$

$$u_{21} = \gamma_{1s}\gamma_{2s}(\beta_{1s} - \beta_{2s}), \quad (\text{A9})$$

$$\beta_{1s} - \beta_{2s} = \frac{u_{21}}{\gamma_{1s}\gamma_{2s}}. \quad (\text{A10})$$

#### A2. DERIVATION OF EQUATION (8)

Let us define (Kennel & Coroniti 1984)

$$Y \equiv \frac{B_{2s}}{B_{1s}} = \frac{\gamma_{2s}u_{1s}}{\gamma_{1s}u_{2s}} = \frac{\beta_{1s}}{\beta_{2s}}; \quad (\text{A11})$$

then equations (3) and (4) can be rewritten as

$$\gamma_{1s}\mu_1[1 + (1 - Y)\sigma] = \gamma_{2s}\mu_2, \tag{A12}$$

$$u_{1s}\mu_1 \left[ 1 + \frac{\sigma}{2\beta_{1s}^2}(1 - Y^2) \right] = u_{2s}\mu_2 + \frac{p_2}{n_2u_{2s}}. \tag{A13}$$

Multiplying equation (A12) by  $\beta_{1s}$  and substituting the resultant formula into equation (A13), one can derive

$$\begin{aligned} \frac{n_2m_p c^2 + e_2}{n_2} &= \left\{ \gamma_{1s}\gamma_{2s}[1 + (1 - Y)\sigma] - u_{1s}u_{2s} \left[ 1 + \frac{\sigma}{2}(\beta_{1s}^{-2} - \beta_{2s}^{-2}) \right] \right\} \mu_1 \\ &= \left( \gamma_{21} - \frac{u_{21}^2}{2u_{1s}u_{2s}} \sigma \right) \mu_1. \end{aligned} \tag{A14}$$

Equation (8) in the text can be then derived straightforwardly.

### A3. SOLVING $u_{2s}^2$

Combining equation (A12) and the definition of  $\mu_2$  (eq. [5]), one can derive

$$\frac{\gamma_{1s}}{\gamma_{2s}}[1 + (1 - Y)\sigma] = 1 + \hat{\Gamma}(\gamma_{21} - 1) - \hat{\Gamma} \frac{u_{21}^2}{2u_{1s}u_{2s}} \sigma. \tag{A15}$$

This turns out to be a three-order equation of  $x \equiv u_{2s}^2$ , i.e.,

$$Ax^3 + Bx^2 + Cx + D = 0, \tag{A16}$$

where

$$A = \hat{\Gamma}(2 - \hat{\Gamma})(\gamma_{21} - 1) + 2, \tag{A17}$$

$$B = -(\gamma_{21} + 1)[(2 - \hat{\Gamma})(\hat{\Gamma}\gamma_{21}^2 + 1) + \hat{\Gamma}(\hat{\Gamma} - 1)\gamma_{21}]\sigma - (\gamma_{21} - 1)[\hat{\Gamma}(2 - \hat{\Gamma})(\gamma_{21}^2 - 2) + (2\gamma_{21} + 3)], \tag{A18}$$

$$\begin{aligned} C &= (\gamma_{21} + 1) \left[ \hat{\Gamma} \left( 1 - \frac{\hat{\Gamma}}{4} \right) (\gamma_{21}^2 - 1) + 1 \right] \sigma^2 \\ &\quad + (\gamma_{21}^2 - 1) [2\gamma_{21} - (2 - \hat{\Gamma})(\hat{\Gamma}\gamma_{21} - 1)] \sigma + (\gamma_{21} + 1)(\gamma_{21} - 1)^2 (\hat{\Gamma} - 1)^2, \end{aligned} \tag{A19}$$

$$D = -(\gamma_{21} - 1)(\gamma_{21} + 1)^2 (2 - \hat{\Gamma})^2 \frac{\sigma^2}{4}. \tag{A20}$$

For  $\hat{\Gamma} = 4/3$ , the four coefficients could be written equivalently as

$$A = 8\gamma_{21} + 10, \tag{A21}$$

$$B = -(\gamma_{21} + 1)(8\gamma_{21}^2 + 4\gamma_{21} + 6)\sigma - (\gamma_{21} - 1)(8\gamma_{21}^2 + 18\gamma_{21} + 11), \tag{A22}$$

$$C = (\gamma_{21} + 1)(8\gamma_{21}^2 + 1)\sigma^2 + (\gamma_{21}^2 - 1)(10\gamma_{21} + 6)\sigma + (\gamma_{21} + 1)(\gamma_{21} - 1)^2, \tag{A23}$$

$$D = -(\gamma_{21} - 1)(\gamma_{21} + 1)^2 \sigma^2. \tag{A24}$$

#### A3.1. $\sigma = 0$ Limit

When  $\sigma = 0$ , equation (A16) is reduced to

$$x[x - (\gamma_{21}^2 - 1)] \{ [\hat{\Gamma}(2 - \hat{\Gamma})(\gamma_{21} - 1) + 2]x - (\gamma_{21} - 1)(\hat{\Gamma} - 1)^2 \} = 0, \tag{A25}$$

which gives equation (12) besides the other two nonphysical solutions  $u_{2s} = 0$  and  $u_{2s} = u_{21}$ .

#### A3.2. $\gamma_{21} \gg 1$ Limit

When  $\gamma_{21} \gg 1$ , the  $x^3$  term is a small quantity and is negligible. Equation (A16) is reduced to

$$\hat{\Gamma}(2 - \hat{\Gamma})(\sigma + 1)x^2 - \left[ \hat{\Gamma} \left( 1 - \frac{\hat{\Gamma}}{4} \right) \sigma^2 + (\hat{\Gamma}^2 - 2\hat{\Gamma} + 2)\sigma + (\hat{\Gamma} - 1)^2 \right] x + (2 - \hat{\Gamma})^2 \frac{\sigma^2}{4} = 0. \tag{A26}$$

This gives the solution (17) in the text (when the nonphysical solution is neglected).

## APPENDIX B

## NOTATION LIST

The notation we used is listed in Table 1.

TABLE 1  
NOTATION LIST

Symbol	Definition
Subscript 1 .....	Upstream (§ 2 and Appendix A), or unshocked medium (§§ 3 and 4)
Subscript 2 .....	Downstream (§ 2 and Appendix A), or shocked medium (§§ 3 and 4)
Subscript 3 .....	Shocked ejecta
Subscript 4 .....	Unshocked ejecta
Subscript $s$ .....	Shock
$c$ .....	Speed of light
$e_i$ .....	Internal energy density in region $i$ ( $=1, 2, 3, 4$ )
$f_a$ .....	Correction factor of $(e_2/n_2 m_p c^2)$ normalized to the $\sigma = 0$ value
$f_b$ .....	Correction factor of $(n_2/n_1)$ normalized to the $\sigma = 0$ value
$f_c$ .....	Magnetic-to-thermal pressure ratio plus 1
$g_f$ .....	$(p_f - 2)/(p_f - 1)$
$g_r$ .....	$(p_r - 2)/(p_r - 1)$
$l$ .....	Sedov length
$m_e$ .....	Electron rest mass
$m_p$ .....	Proton rest mass
$n_i$ .....	Baryon number density in region $i$ ( $=1, 2, 3, 4$ )
$p_i$ .....	Thermal pressure in region $i$ ( $=1, 2, 3, 4$ )
$p_{b,i}$ .....	Magnetic pressure in region $i$ ( $=1, 2, 3, 4$ )
$p_f$ .....	Electron power-law index in the forward shock
$p_r$ .....	Electron power-law index in the reverse shock
$t_{\text{dec}}$ .....	Deceleration time measured by the observer
$t_\gamma$ .....	$R_\gamma/C_\gamma \gamma_4^2 c$ (eq. [48])
$t_{p,f}$ .....	Emission peak time of the forward shock component
$t_{p,r}$ .....	Emission peak time of the reverse shock component
$t_\times$ .....	Shock crossing time measured by the observer
$u_{ij}$ .....	Four speed in the region $i$ ( $=1, 2, 3, 4$ ) in the rest frame of $j$ ( $=1, 2, 3, 4, s$ )
$x$ .....	$u_{2s}^2$
$y$ .....	Pair multiplicity parameter
$z$ .....	Redshift
$A, B, C, D$ .....	Coefficients to solve the equation for $u_{2s}^2$
$B_i$ .....	Comoving magnetic field in the region $i$ ( $=1, 2, 3, 4$ )
$B_{is}$ .....	Magnetic field in the region $i$ ( $=1, 2, 3, 4$ ) in the rest frame of the shock
$B_f$ .....	Comoving magnetic field in the forward shocked region
$B_r$ .....	Comoving magnetic field in the reverse shocked region
$C_N$ .....	Correction factor to $R_N$ with respect to the $\sigma = 0$ case
$C_\Delta$ .....	Correction factor to $R_\Delta$ with respect to the $\sigma = 0$ case
$C_\gamma$ .....	Correction factor to $R_\gamma$ with respect to the $\sigma = 0$ case
$\mathcal{E}$ .....	Shock frame electric field
$E$ .....	Isotropic total energy of the fireball
$E_K$ .....	Isotropic kinetic energy of the fireball
$E_P$ .....	Isotropic Poynting flux energy of the fireball
$F$ .....	The product of $f_a, f_b$ , and $f_c$
$F_\nu$ .....	Specific flux at the frequency $\nu$
$F_{\nu,m,f}$ .....	Maximum synchrotron emission specific flux in the forward shock
$F_{\nu,m,r}$ .....	Maximum synchrotron emission specific flux in the reverse shock
$F_{\nu,p,f}$ .....	Peak flux for the forward shock emission component in certain (e.g., $R$ ) band
$F_{\nu,p,r}$ .....	Peak flux for the reverse shock emission component in certain (e.g., $R$ ) band
$H_0$ .....	Hubble constant
$M_0$ .....	Mass in the ejecta
$M_{\text{ISM}}$ .....	Mass of the interstellar medium collected by the shock
$N_b$ .....	Total baryon number in the shell
$N_\pm$ .....	Total electron-positron pair number in the shell
$N_{e,f}$ .....	Lepton (electron) number in the forward shock
$N_{e,r}$ .....	Lepton (electron and pairs) number in the reverse shock
$Q$ .....	A parameter introduced to categorize the parameter regimes (defined by eq. [50])
$R$ .....	Radius from the central engine
$\mathcal{R}_B$ .....	Reverse-to-forward comoving magnetic field ratio
$\mathcal{R}_e$ .....	Reverse-to-forward ratio of the $\epsilon_e g$ parameter
$\mathcal{R}_F$ .....	Reverse-to-forward peak flux ratio
$\mathcal{R}_t$ .....	Forward-to-reverse peak time ratio

TABLE 1—Continued

Symbol	Definition
$\mathcal{R}_\nu$ .....	The ratio between $\nu_R$ and $\nu_{m,r}(t_{dec})$
$R_N$ .....	Radius where the reverse shock becomes relativistic
$R_S$ .....	Radius where the ejecta shell starts to spread
$R_\Delta$ .....	Radius where the reverse shock crosses the ejecta shell
$R_\gamma$ .....	Radius where the fireball collects $1/\gamma_0$ rest mass of the fireball
$T$ .....	Central engine activity timescale
$U_{B,0}$ .....	Initial comoving magnetic energy
$U_B$ .....	Comoving magnetic energy after shock crossing
$X$ .....	An intermediate parameter introduced in equation (17)
$Y$ .....	Ratio between $B_{2s}$ and $B_{1s}$
$\hat{\Gamma}$ .....	Adiabatic index
$\Delta$ .....	Shell width in the lab frame
$\Delta_0$ .....	Initial shell width in the lab frame
$\Omega_m$ .....	Cosmology mass density parameter
$\Omega_\Lambda$ .....	Cosmology $\Lambda$ density parameter
$\alpha$ .....	Temporal decay index of the reverse shock emission component after peak time
$\beta_{ij}$ .....	Dimensionless velocity of region $i$ ( $=1, 2, 3, 4$ ) in the rest frame of $j$ ( $=1, 2, 3, 4, s$ )
$\hat{\gamma}$ .....	An equivalent Lorentz factor defined in eq. (74)
$\gamma_{ij}$ .....	Lorentz factor of region $i$ ( $=1, 2, 3, 4$ ) in the rest frame of $j$ ( $=1, 2, 3, 4, s$ )
$\gamma_i$ .....	Lorentz factor of region $i$ ( $=2, 3, 4$ ) in the rest frame of the circumburst medium
$\gamma_0$ .....	Initial Lorentz factor of the fireball, $\gamma_0 \equiv \gamma_4$
$\gamma_c$ .....	Critical initial Lorentz factor that separates thick vs. thin shell regimes (eq. [52])
$\gamma_\times$ .....	Fireball Lorentz factor at the shock crossing time
$\gamma_{e,m,f}$ .....	Electron minimum Lorentz factor in the forward shock
$\gamma_{e,m,r}$ .....	Electron minimum Lorentz factor in the reverse shock
$\epsilon_{e,f}$ .....	Electron energy equipartition parameter in the forward shock
$\epsilon_{e,r}$ .....	Electron energy equipartition parameter in the reverse shock
$\epsilon_{B,f}$ .....	Magnetic energy equipartition parameter in the forward shock
$\bar{\epsilon}_{B,r}$ .....	Equivalent magnetic energy equipartition parameter in the reverse shock
$\mu_i$ .....	Specific enthalpy in region $i$ ( $=1, 2, 3, 4$ )
$\nu_{c,f}$ .....	Forward shock synchrotron cooling frequency
$\nu_{c,r}$ .....	Reverse shock synchrotron cooling frequency
$\nu_{m,f}$ .....	Forward shock synchrotron typical frequency
$\nu_{m,r}$ .....	Reverse shock synchrotron typical frequency
$\nu_R$ .....	$R$ -band frequency
$\xi$ .....	A parameter defined in eq. (45)
$\xi_0$ .....	The $\xi$ value when $\Delta = \Delta_0$
$\sigma$ .....	Magnetization parameter as defined in eq. (7)

## REFERENCES

- Achterberg, A., Gallant, Y. A., Kirk, J. G., & Guthmann, A. W. 2001, *MNRAS*, 328, 393
- Akerlof, C. W., et al. 1999, *Nature*, 398, 400
- Blandford, R. D. 2002, in *Lighthouses of the Universe: The Most Luminous Celestial Objects and Their Use for Cosmology*, ed. M. Gilfanov, R. A. Suniaev, & E. Churazov (Berlin: Springer), 381
- Blandford, R. D., & Eichler, D. 1987, *Phys. Rep.*, 154, 1
- Blandford, R. D., & McKee, C. F. 1976, *Phys. Fluids*, 19, 1130
- Chevalier, R. A., & Li, Z.-Y. 2000, *ApJ*, 536, 195
- Coburn, W., & Boggs, S. E. 2003, *Nature*, 423, 415
- Covino, S., Ghisellini, G., Lazzati, D., & Malesani, D. 2003, preprint (astro-ph/0301608)
- Dermer, C. D., & Mitman, K. E. 1999, *ApJ*, 513, L5
- Double, G. P., Baring, M. G., Jones, F. C., & Ellison, D. C. 2004, *ApJ*, 600, 485
- Drenkhahn, G., & Spruit, H. C. 2002, *A&A*, 391, 1141
- Fan, Y. Z., Dai, Z. G., Huang, Y. F., & Lu, T. 2002, *Chinese J. Astron. Astrophys.*, 2, 449
- Fan, Y. Z., Wei, D. M., & Wang, C. F. 2004a, *A&A*, 424, 477
- Fan, Y. Z., Wei, D. M., & Zhang, B. 2004b, *MNRAS*, 354, 1031
- Fermi, E. 1949, *Phys. Rev.*, 75, 1169
- Fox, D. W., et al. 2003a, *Nature*, 422, 284
- . 2003b, *ApJ*, 586, L5
- Gallant, Y. A., Hoshino, M., Langdon, A. B., Arons, J., & Max, C. E. 1992, *ApJ*, 391, 73
- Granot, J. 2003, *ApJ*, 596, L17
- Granot, J., & Königl, A. 2003, *ApJ*, 594, L83
- Kennel, C. F., & Coroniti, F. V. 1984, *ApJ*, 283, 694
- Kobayashi, S. 2000, *ApJ*, 545, 807
- Kobayashi, S., Mészáros, P., & Zhang, B. 2004, *ApJ*, 601, L13
- Kobayashi, S., Piran, T., & Sari, R. 1999, *ApJ*, 513, 669
- Kobayashi, S., Ryde, F., & MacFadyen, A. I. 2002, *ApJ*, 577, 302
- Kobayashi, S., & Sari, R. 2000, *ApJ*, 542, 819
- Kobayashi, S., & Zhang, B. 2003a, *ApJ*, 582, L75
- . 2003b, *ApJ*, 597, 455
- Kumar, P., & Panaitescu, A. 2003, *MNRAS*, 346, 905
- Li, W., Filippenko, A. V., Chornock, R., & Jha, S. 2003a, *ApJ*, 586, L9
- Li, Z., Dai, Z. G., Lu, T., & Song, L. M. 2003b, *ApJ*, 599, 380
- Li, Z.-Y., & Chevalier, R. A. 2003, *ApJ*, 589, L69
- Lloyd-Ronning, N. M., & Zhang, B. 2004, *ApJ*, 613, 477
- Lyutikov, M., & Blandford, R. C. 2003, *ApJ*, submitted (astro-ph/0312347)
- MacFadyen, A. I., & Woosley, S. E. 1999, *ApJ*, 524, 262
- Medvedev, M. V., & Loeb, A. 1999, *ApJ*, 526, 697
- Mészáros, P. 2002, *ARA&A*, 40, 137
- Mészáros, P., Ramirez-Ruiz, E., Rees, M. J., & Zhang, B. 2002, *ApJ*, 578, 812
- Mészáros, P., & Rees, M. J. 1993, *ApJ*, 405, 278
- . 1997a, *ApJ*, 476, 232
- . 1997b, *ApJ*, 482, L29
- Nakar, E., & Piran, T. 2004, *MNRAS*, 353, 647
- Panaitescu, A., & Kumar, P. 2002, *ApJ*, 571, 779
- Proga, D., MacFadyen, A. I., Armitage, P. J., & Begelman, M. C. 2003, *ApJ*, 599, L5
- Rees, M. J., & Mészáros, P. 1994, *ApJ*, 430, L93
- Rutledge, R. E., & Fox, D. B. 2004, *MNRAS*, 350, 1288
- Rykoff, E. S., et al. 2004, *ApJ*, 601, 1013
- Sagiv, A., Waxman, E., & Loeb, A. 2004, *ApJ*, 615, 366
- Sari, R., & Piran, T. 1995, *ApJ*, 455, L143
- . 1999, *ApJ*, 520, 641

- Sari, R., Piran, T., & Narayan, R. 1998, *ApJ*, 497, L17  
Spitkovsky, A., & Arons, J. 2004, *ApJ*, 603, 669  
Spruit, H. C., Daigne, F., & Drenkhahn, G. 2001, *A&A*, 369, 694  
Thompson, C. 1994, *MNRAS*, 270, 480  
Usov, V. V. 1994, *MNRAS*, 267, 1035  
Wang, X. Y., Wu, X. F., Fan, Y. Z., Dai, Z. G., & Zhang, B. 2005, *ApJ*, 623, L29  
Waxman, E. 2003, *Nature*, 423, 388  
Wheeler, J. C., Yi, I., Höflich, P., & Wang, L. 2000, *ApJ*, 537, 810  
Wu, X. F., Dai, Z. G., Huang, Y. F., & Lu, T. 2003, *MNRAS*, 342, 1131  
Yost, S., Harrison, F. A., Sari, R., & Frail, D. A. 2003, *ApJ*, 597, 459  
Zhang, B., & Kobayashi, S. 2005, preprint (astro-ph/0504425)  
Zhang, B., Kobayashi, S., & Mészáros, P. 2003, *ApJ*, 595, 950 (ZKM03)  
Zhang, B., & Mészáros, P. 2002, *ApJ*, 581, 1236  
———. 2004, *Int. J. Mod. Phys. A*, 19, 2385